Autolamellasomes: Linking Autophagy-Dependent ER Degradation to Whorled Lysosome Biogenesis

Di Lu[1*], Rouxuan Zhang[2], Wanjing Shi[1], Delin Zhan[1], Yuntian Yang[1], Xulin Sun[1], Han Zhang[1], Ying Li[3], Xueming Li[2] and Li Yu[1*]

[1]The State Key Laboratory of Membrane Biology, Tsinghua University-Peking University Joint Center for Life Sciences, Beijing Frontier Research Center for Biological Structure, School of Life Sciences, Tsinghua University, Beijing 100084, China.

[2]The State Key Laboratory of Membrane Biology, Tsinghua University-Peking University Joint Center for Life Sciences, Beijing Frontier Research Center for Biological Structure, MOE Key Laboratory of Protein Sciences, School of Life Sciences, Tsinghua University, Beijing 100084, China.

[3]Technology Center for Protein Sciences, School of Life Sciences, Tsinghua University, Beijing, China.

* Correspondence: Li Yu, liyulab@mail.tsinghua.edu.cn;

Di Lu, ld2023@mail.tsinghua.edu.cn

Abstract

Lysosomes containing multilamellar membrane whorls are a hallmark of cellular aging and storage disorders, yet the biogenesis of these structures has remained elusive for decades. Here, we identify a distinct form of endoplasmic reticulum (ER) remodeling, termed autolamellasomes, which mediates bulk ER degradation under chronic mTOR inhibition. Unlike canonical ER-phagy, autolamellasomes are concentric ER stacks that form via an autophagy-dependent but receptor-independent mechanism. Using Cryo-ET, CLEM, and a reconstituted cell-free system, we demonstrate that these structures arise from the cytosolic compaction of fragmented ER membranes, driven by the core autophagy machinery. We find that autolamellasomes accumulate in senescent cells and fibroblasts from patients with Hutchinson-Gilford progeria syndrome, linking sustained

mTOR suppression to lysosomal membrane homeostasis. Our results resolve the origin of intralysosomal whorls and define a conserved pathway that couples nutrient sensing to membrane turnover and cellular aging.

Key words

Autolamellasome, Autophagy, ER, Lysosome, mTOR

Introduction

Autophagy is an evolutionarily conserved catabolic process essential for eukaryotic homeostasis[1-4]. By sequestering cytoplasmic components—from macromolecules to organelles—into double-membrane autophagosomes for lysosomal degradation, this pathway recycles nutrients during starvation and eliminates damaged structures[5-7]. Although originally viewed as a non-selective bulk response to nutrient deprivation, autophagy is now understood as a precisely regulated, selective system[8]. Distinct pathways, such as mitophagy and aggrephagy, target specific substrates via cargo receptors that bridge cargo to the autophagic machinery through LC3-interacting region (LIR) motifs[9-11].

A paradigm of this selectivity is endoplasmic reticulum (ER) autophagy (ER-phagy), which regulates ER size and function through lysosomal turnover[12]. As the site of protein synthesis and lipid metabolism, ER homeostasis is critical for cell survival[13,14]. ER-phagy operates via distinct morphological routes, including micro-ER-phagy and vesicular transport, but is primarily driven by receptor-mediated macro-ER-phagy[15-17]. Specific transmembrane receptors, such as FAM134B and RTN3L, govern the specificity of this process. Beyond functioning as tethers, these receptors utilize reticulon homology domains to actively remodel and fragment ER sheets or tubules, facilitating their sequestration by the phagophore. FAM134B preferentially targets ER sheets, whereas RTN3L and ATL3 act on tubules[18-21]. Others, such as CCPG1, also

recruit upstream autophagy regulators (e.g., FIP200), directly initiating local autophagosome formation at the ER surface[22,23]. Collectively, these mechanisms ensure the spatiotemporal precision of ER turnover.

Lysosomes characteristically contain dense, lamellar structures composed of membrane whorls and intraluminal vesicles[24]. While such multilamellar bodies—including myelin figures and zebra bodies—are hallmarks of lysosomal storage disorders and drug-induced phospholipidosis[25-29], their biophysical origins remain obscure. Although it is hypothesized that these structures arise when lipid-rich cargo resists degradation[30], the mechanisms governing their initiation and persistence are largely undefined.

Distinct multilamellar ER whorls also emerge under severe ER stress. In yeast, these structures are cleared via ESCRT-dependent micro-ER-phagy, independent of core autophagy genes (ATGs)[16]. Similarly, mammalian cells form massive COPII-dependent ER whorls to sequester translocons and alleviate stress; these, too, are generated and cleared independently of canonical autophagy[31].

Here, we identify a distinct mechanism of ER remodeling driven by chronic mTOR inhibition. We report the discovery of "autolamellasomes"—extensive, multilamellar structures composed of densely packed, concentric ER membranes. Unlike canonical autophagosomes, autolamellasomes form via a unique pathway that requires the core autophagy machinery yet proceeds independently of all known ER-phagy receptors. Using cell-free reconstitution and genetic analyses, we demonstrate that autolamellasomes arise from the compaction of fragmented ER membranes to facilitate bulk ER degradation under prolonged nutrient stress. Furthermore, these structures accumulate in senescent cells and fibroblasts from patients with Hutchinson-Gilford progeria syndrome (HGPS). These findings define autolamellasomes as a parallel, receptor-independent architecture for ER turnover, linking mTOR signaling to membrane homeostasis and cellular aging.

Results

Prolonged mTOR Inhibition Induces the Formation of “Free Whorls”

While acute mTOR inhibition is known to induce transient autophagosome formation, we found that prolonged treatment (24 h) with Torin1 resulted in a distinct ultrastructural phenotype: the accumulation of dense, whorl-like membrane structures (0.5–2 μm) within autolysosomes, rather than typical autophagosomes (Fig. 1a). Strikingly, we also identified abundant multilamellar structures residing in the cytosol that lacked a limiting membrane. These structures, which we termed "free whorls," were composed of stacked double membranes and morphologically resembled the intralysosomal whorls (Fig. 1b).

Free whorls were frequently localized in close proximity to the endoplasmic reticulum (ER). Kinetic analysis revealed that free whorls emerged as early as 4 hours post-treatment and accumulated progressively. This cytosolic accumulation was temporally synchronized with the increase in whorl-containing lysosomes and the number of whorls per lysosome (Fig. 1c, d), suggesting a precursor-product relationship. This phenomenon was conserved across diverse species and distinct modes of mTOR inhibition, including rapamycin and starvation (Fig. 1h; Extended Data Fig. 1a, m-o).

To resolve the native architecture of these structures, we employed cryo-electron tomography (cryo-ET). This analysis unambiguously confirmed that free whorls are organized as concentric stacks of double membranes with a regular luminal spacing of ~15 nm (Fig. 1e, f). Furthermore, three-dimensional FIB-SEM further demonstrated that each whorl forms a spherical structure (Fig. 1g). Collectively, these data indicate that sustained mTOR suppression triggers the biogenesis of cytosolic free whorls, which are subsequently internalized by lysosomes.

112 **The Free Whorls Originate from the ER and mediate bulk ER turnover**

113

114 Given the frequent association of free whorls with the endoplasmic reticulum (ER), we
115 investigated whether these structures are ER-derived. Live-cell imaging revealed a
116 dramatic topological transition of the ER from a continuous reticular network to
117 discrete punctate structures following prolonged mTOR inhibition (Fig. 2a, b). These
118 ER-derived puncta were consistently observed using multiple ER markers (REEP5,
119 SEC61B, Calnexin) and diverse labeling strategies (fluorescent tags and endogenous
120 immunostaining), confirming that this phenotype is independent of specific tags or
121 expression levels (Fig. 2c-k; Extended Data Fig. 1b-i). While overexpression slightly
122 enhanced puncta frequency, endogenous proteins displayed an identical redistribution
123 pattern into lysosomes.

124

125 To definitively resolve the ultrastructure of these puncta, we employed APEX2-based
126 electron microscopy and correlative light and electron microscopy (CLEM). Both
127 APEX2-SEC61B and APEX2-REEP5 specifically labeled the electron-dense whorls,
128 and CLEM confirmed the precise colocalization of fluorescent REEP5 signals with
129 these multilamellar structures (Fig. 2l, m; Extended Data Fig. 1m). Live-cell time-lapse
130 imaging further captured the dynamics of this process, revealing the rapid emergence
131 of ER puncta and their progressive accumulation within LAMP1^{+} autolysosomes (Fig.
132 2n; Extended Data Fig. 1j, k). Collectively, these data provide direct evidence that
133 autolamellasomes originate from the remodeling of ER membranes.

134

135 Consistent with this morphological remodeling, biochemical analysis revealed
136 progressive degradation of the ER proteome. Prolonged mTOR inhibition led to the
137 widespread turnover of ER-resident proteins, as quantified by both Western blotting
138 and label-free mass spectrometry (Fig. 2o-q). Interestingly, degradation kinetics
139 revealed distinct temporal profiles across substrates: the autophagy substrate p62 was
140 rapidly cleared (<4 h), whereas ER-resident proteins exhibited heterogeneous turnover

rates. FAM134B declined sharply, REEP5 and ATL3 remained stable for up to 12 hours before undergoing abrupt loss, while others degraded gradually or showed minimal turnover (e.g., TEX264) (Fig. 2r, s). Here, we observed discrepancies between mass spectrometry and Western blot data for select proteins. Notably, TEX264 showed a modest reduction by quantitative mass spectrometry but a slight increase by Western blot, likely reflecting differential detection of distinct protein pools or technical variations in antibody specificity.

Together, these data indicate that prolonged mTOR inhibition induces the formation of ER-derived puncta, which are subsequently engulfed and degraded by autolysosomes/lysosomes (Fig. 2t). The distinct kinetics and selectivity of degradation suggest that multiple mechanisms—including transcriptional regulation, selective ER-phagy, and puncta formation—contribute to the turnover of ER components under sustained mTOR inhibition.

Formation of Whorls Depends on the Core Autophagy Machinery but Not ER-Phagy Receptors

To define the genetic architecture of whorl formation, we first interrogated the role of known ER-phagy receptors. Surprisingly, individual deletion of major receptors—including FAM134B[18], SEC62[32], TEX264[33,34], ATL3[21], and CCPG1[23]—did not affect whorl formation. To rigorously exclude redundancy, we generated a "penta-knockout" line (ERphR-KO) lacking all five known receptors (FAM134B, ATL3, SEC62, TEX264, and CCPG1). Across three independently derived clones, simultaneous loss of these receptors had minimal impact on whorl formation. We then asked whether genes implicated in the generation of large ER whorls (~10 μm) under ER stress conditions might contribute. Similarly, ablating key UPR (unfolded protein response) regulators or genes implicated in ER stress-induced whorls had no detectable effect (Fig. 3a).

We next tested genes involved in general membrane dynamics based on functional prediction. Among these, knockout of NPC2 modestly reduced whorl formation, whereas deletion of PI4KIIA, VPS13C, or SCAP had no discernible effect. In striking contrast, disruption of core autophagy genes markedly impaired whorl biogenesis. Deletion of ATG2 (ATG2A/2B DKO), ATG7, ATG9A, or ATG8 (mammalian LC3/GABARAP family) almost completely abolished whorl biogenesis, while loss of ATG5, ATG14, ATG13, ATG16L, or ATG3 resulted in moderate reductions. Knockout of Beclin-1 or WIPI2 had a weak effect, and deletion of ULK1 or p62 showed no significant impact (Fig. 3a). Together, these results demonstrate that the core autophagy machinery—but not canonical ER-phagy receptors—is essential for whorl formation.

We next assessed how disruption of these pathways affects ER protein turnover. Two complementary assays were employed. First, we monitored cleavage of mCherry-REEP5, a well-established reporter for ER-phagy. Knockout of autophagy core components—including ATG2, ATG5, and ATG7—completely blocked mCherry-REEP5 cleavage (Fig. 3b, c). In contrast, deletion of individual ER-phagy receptors (FAM134B, SEC62, ATL3) had no significant effect, while TEX264 and CCPG1 knockouts modestly reduced cleavage efficiency (Extended Fig. 2a-c). Second, we examined endogenous ER protein degradation. Core autophagy gene deletion broadly prevented degradation of multiple ER proteins, whereas ERphR-KO and individual ER-phagy receptor knockout cells exhibited normal degradation (Fig. 3b, d, e, Extended Fig. 2a, d, e). Collectively, these findings indicate that degradation of ER components under prolonged mTOR inhibition depends primarily on the core autophagy machinery, rather than on specific ER-phagy receptors.

We next analyzed ER morphology in cells lacking essential autophagy genes. ER translocation into autolysosomes and autolysosomal whorls were abolished in ATG2, ATG5, ATG7 and ATG8-hexa knockout cells (Fig. 3f-i, Extended Fig. 2f, g, m-p), whereas ERphR-KO did not affect whorl formation (Fig. 3j, k, Extended Fig. 2h, i).

199 Consistent with the genetic data, ER puncta in wild-type cells were positive for LC3
200 (Extended Fig. 2j-l), and notably, they exhibited strong ATG9A signal—a feature
201 distinct from canonical autophagosomes, which typically display transient or weak
202 ATG9A labeling[35,36] (Fig. 3l, m). Triple labeling with BFP-LC3, mCherry-REEP5, and
203 LAMP1-YFP revealed two distinct maturation stages: "free whorls"
204 ($REEP5^+/LC3^+/LAMP1^-$) and internalized whorls ($REEP5^+/LC3^+/LAMP1^+$) (Fig. 3n).
205 APEX2 labeling further confirmed these observations at the ultrastructural level,
206 revealing LC3-positive autophagosomes, ER fragments, multilamellar whorls, and
207 whorls enclosed within autolysosomes (Fig. 3o, p).
208
209 Collectively, these data demonstrate that the formation of these structures is driven by
210 the core autophagy machinery but operates independently of canonical ER-phagy
211 receptors (Fig. 3q). Based on these findings, we designate these structures
212 “autolamellasomes”, reflecting both their dependence on autophagy machinery and
213 their distinctive multilamellar morphology. This nomenclature also distinguishes them
214 from classical ER whorls generated under ER-stress conditions.
215
216 **Autolamellasomes Form via Autophagy-Dependent Assembly of ER Fragments**
217
218 To dissect the cellular mechanics of assembly, we utilized oleic acid (OA) followed by
219 prolonged mTOR inhibition (Fig. 4a). Unexpectedly, in addition to promoting lipid
220 droplet formation[37], OA treatment triggered a profound reorganization of ER
221 architecture, manifested by the redistribution of REEP5 into large, dynamic "ER
222 patches" in both wild-type and autophagy-deficient (ATG2, ATG5, and ATG7-deficient)
223 cells (Fig. 4b). Fluorescence recovery after photobleaching (FRAP) experiments
224 showed rapid recovery of mCherry-REEP5 signal within these patches, indicating
225 lateral diffusion of ER fragments across patch boundaries—a behavior reminiscent of
226 liquid-like properties (Extended Fig. 4a, b).
227

228 We then tracked the fate of these structures under mTOR inhibition. In wild-type NRK
229 cells, time-lapse imaging captured the direct conversion of ER patches into compact
230 autolamellasomes (Extended Fig. 4c). In striking contrast, loss of core autophagy genes
231 (ATG2, ATG5, ATG7) completely decoupled patch formation from whorl assembly:
232 while ER patches continued to enlarge in these mutants, they failed to organize into
233 autolamellasomes (Fig. 4b-d). Notably, this blockage was absolute in ATG2- and ATG7-
234 deficient cells, whereas ATG5 knockout resulted in a partial phenotype, suggesting
235 distinct hierarchical roles for these proteins. Interestingly, while OA treatment induced
236 ER patches in most wild-type and ATG2-deficient cells, this response was initially
237 restricted to a subset of ATG5- and ATG7-deficient cells. However, prolonged mTOR
238 inhibition led to the accumulation of enlarged ER patches across all autophagy-deficient
239 backgrounds. These findings suggest that while ATG5 and ATG7 may differentially
240 regulate initial patch dynamics, the core autophagy machinery is fundamentally
241 required to convert these ER precursors into autolamellasomes
242
243 To further characterize the nature of ER patches, we performed correlative light and
244 electron microscopy (CLEM), which revealed that these patches consist of clustered
245 ER fragments (Fig. 4e), consistent with their rapid fluorescence recovery after
246 photobleaching. TEM analysis showed abundant autolamellasomes either free in the
247 cytoplasm or enclosed within autolysosomes in wild-type cells, whereas autophagy-
248 deficient cells accumulated disordered ER fragments instead (Fig. 4f, g). APEX2
249 labeling of SEC61B confirmed that in wild-type cells, autolamellasomes emerged
250 directly from ER fragment clusters, reflecting the assembly of ordered multilamellar
251 structures from disordered ER components. In contrast, almost no autolamellasome
252 structures were detected in autophagy-deficient cells (Fig. 4h, i).
253
254 Together, these data demonstrate that autolamellasomes arise through the autophagy-
255 dependent assembly of ER fragments, with the core autophagy machinery orchestrating
256 their transformation from disordered ER clusters into organized multilamellar

structures (Fig. 4j).

In Vitro Reconstitution of Autolamellasome Biogenesis

To demonstrate that cytosolic factors and the core autophagy machinery are sufficient to drive autolamellasome assembly, we established a cell-free reconstitution system using digitonin-permeabilized semi-intact cells (Fig. 5a). The assay was conceptually adapted from the classic COPII-budding assay developed by Schekman and Novick, which uses permeabilized cells to study vesicle formation[38,39]. However, instead of collecting released vesicles, we monitored the formation of autolamellasomes within permeabilized cells by transmission electron microscopy. In this assay, acceptor membranes were prepared from cells pre-expanded with oleic acid. Reconstitution was assessed using various protocols: a simultaneous method, where permeabilization and factor supplementation occurred concurrently; and a sequential method, where endogenous cytosol was depleted prior to the addition of exogenous S150, ATP, and GTP (Fig. 5b). Rigorous quality control confirmed the complete loss of plasma membrane, lysosomal and microtubule integrity, ensuring that any observed structures were formed *de novo* rather than representing pre-existing lysosomal whorls (Extended Data Fig. 5a-o).

Electron microscopy revealed striking differences between control and reconstituted samples. In control preparations, internal membrane structures were extensively disrupted. In contrast, samples containing cytosol and nucleotides displayed numerous autolamellasomes at various stages of formation, as well as autophagosomes (Fig. 5c-e). Compared with TEM analysis of intact cells, the proportion of free autolamellasomes was substantially increased, suggesting efficient reconstitution of their formation within permeabilized cells.

We next examined the dependence on ATG7. Using ATG7-deficient cells as the

286 membrane source, addition of wild-type S150 cytosol partially rescued
287 autolamellasome formation to ~60 % of wild-type efficiency. Surprisingly, cytosol
288 derived from ATG7-deficient cells still supported low-level formation—about one-third
289 of wild-type levels—indicating that while ATG7 is indispensable for autolamellasome
290 formation *in vivo*, limited assembly can occur *in vitro* (Fig. 5f-h).
291
292 Together, these results establish a foundational cell-free system that captures the
293 essential process of autolamellasome and autophagosome biogenesis. This *in vitro*
294 approach reveals a core mechanistic principle: the formation of these structures is
295 driven by soluble cytosolic factors acting upon permeabilized cellular membranes.
296 Furthermore, the system demonstrates that while the core component ATG7 is a major
297 accelerator of autolamellasome formation, the process retains a basal, ATG7-
298 independent capacity. This suggests the existence of either alternative, low-efficiency
299 pathways or a residual self-organizing potential within the membrane itself that can be
300 co-opted by the cytosol to initiate this form of membrane remodeling.
301
302 **Autolamellasome accumulation is a conserved signature of cellular aging and**
303 **progeria**
304
305 Intralysosomal membrane whorls are a ubiquitous ultrastructural feature of lysosomes,
306 yet their origin has remained obscure. We hypothesized that these structures represent
307 the terminal stage of basal autolamellasome formation. Indeed, electron microscopy
308 and immunostaining revealed the presence of autolamellasomes at basal levels across a
309 diverse array of immortalized cell lines, primary cultures, and murine tissues,
310 identifying this pathway as a constitutive mechanism for bulk ER turnover *in vivo* (Fig.
311 6a, b, Extended Fig. 6a-i).
312
313 To dissect the dynamics of this basal turnover, we perturbed the autophagy-lysosome
314 flux. Under nutrient-rich conditions, ATG7 depletion significantly reduced

autolamellasome frequency, although a residual population persisted, suggesting potential redundancy in basal biogenesis (Extended Fig. 7a-c). Conversely, blocking lysosomal degradation with chloroquine (CQ) triggered a massive accumulation of ER-derived autolamellasomes—verified by ER-Tracker, APEX2 labeling of SEC61B and LC3, and cryo-electron tomography—which failed to form in autophagy-deficient backgrounds (ATG2/5/7 KO) ((Extended Fig. 7d-n). These data definitively resolve the origin of intralysosomal whorls, identifying them as autolamellasomes generated through a constitutive, autophagy-dependent flux.

We next reasoned that the characteristic accumulation of "myelin figures" in aging cells might reflect a dysregulation of this pathway. Using doxorubicin- and oxidative stress-induced senescence models[40,41], we observed a dramatic accumulation of autolamellasomes, whereas autophagy-deficient cells failed to form autolamellasomes and instead accumulated large, irregular ER patches (Fig. 6c-h, Extended Fig. 8a-p). Mechanistically, this accumulation was driven by a dual process: the decline of lysosomal degradative capacity[42] and the active induction of biogenesis via chronic mTOR suppression. Consistent with this, pharmacological activation of mTOR (MHY1485) effectively abolished ER translocation into lysosomes in senescent cells (Fig. 6i-m).

Finally, we extended these findings to Hutchinson–Gilford Progeria Syndrome (HGPS). Patient-derived fibroblasts expressing the mutant lamin A protein, Progerin, displayed extensive autolamellasome accumulation concurrent with suppressed mTOR signaling (Fig. 6n-s). Importantly, inducible expression of Progerin in wild-type cells was sufficient to drive robust, autophagy-dependent autolamellasome formation (Fig. 6t-v, Extended Fig. 9a).

Collectively, these findings position autolamellasome accumulation as a conserved structural signature of aging. This pathway physically connects two hallmarks of the

aging cell—organelle stress and nutrient signaling collapse—demonstrating that the age-associated "whorls" are not merely passive debris, but the product of an active, albeit overwhelmed, membrane remodeling program.

Discussion

This study identifies a distinct mechanism of ER remodeling driven by chronic mTOR inhibition: the formation of autolamellasomes. We show that these multilamellar structures utilize the core autophagy machinery but operate independently of canonical ER-phagy receptors. Unlike conventional autophagosomes, autolamellasomes mediate bulk ER degradation via the compaction and lysosomal incorporation of ER fragments. Their conservation across diverse cell types and their specific accumulation in senescent and HGPS fibroblasts reveal a fundamental, aging-associated pathway linking sustained mTOR suppression to membrane homeostasis. These findings provide a structural framework for understanding how long-term autophagy activation reshapes cellular architecture.

Our results also resolve a longstanding question regarding the origin of intralysosomal membrane whorls—variably termed myelin figures or zebra bodies. We demonstrate that these enigmatic structures originate from basal autolamellasome formation. Ubiquitously detected from cultured cells to mouse embryos, this basal activity likely represents a housekeeping mechanism for steady-state ER turnover. Thus, the identification of autolamellasomes provides a unifying biogenic explanation for lysosomal whorls, establishing a physiological link between ER dynamics, lysosomal structure, and long-term membrane flux.

Mechanistically, the autolamellasome pathway differs fundamentally from previously described ER whorls. In yeast, acute ER stress triggers whorls that are cleared via ESCRT-dependent, ATG-independent micro-ER-phagy. Conversely, severe ER stress in mammalian cells induces large, PERK- and COPII-dependent whorls that sequester

translocons but are not degraded by autophagy. By contrast, autolamellasomes emerge under sustained mTOR inhibition, depend on the core autophagy machinery (but not ER-phagy receptors or UPR signaling), and represent a degradative pathway. This distinction defines a unique route linking nutrient sensing to bulk membrane recycling, separate from both the yeast micro-ER-phagy pathway and the adaptive, non-degradative mammalian stress response.

A critical advance of this study is the establishment of a cell-free system that faithfully recapitulates autolamellasome formation *in vitro*. We demonstrate that multilamellar structures self-organize from cellular membranes in the presence of cytosolic factors and energy cofactors, proving the sufficiency of the core autophagy machinery for this assembly. Analogous to historic reconstitutions of vesicular trafficking, this system transforms a complex cellular process into a tractable biochemical reaction, providing a powerful platform for dissecting the molecular logic of autophagy-driven membrane remodeling at high resolution.

Although we have elucidated the mechanistic framework of autolamellasome biogenesis, the molecular determinants orchestrating their distinctive multilamellar architecture remain to be identified. Systematic, unbiased genetic screens will be paramount to uncovering the regulators governing this assembly, particularly membrane-shaping proteins and lipid-metabolizing enzymes. Crucially, the physiological relevance of autolamellasomes warrants rigorous validation *in vivo*. The development of sophisticated animal models—enabling precise spatiotemporal modulation of autolamellasome formation—will be essential to deciphering their contributions to organ function, stress adaptation, and systemic homeostasis. Given their capacity for extensive membrane remodeling and lipid catabolism, we propose that autolamellasomes serve as an adaptive reservoir for energy recycling during protracted nutrient limitation. Furthermore, their pronounced accumulation in senescent and progeroid contexts suggests that this pathway is a hallmark of the cellular response

402 to aging-associated mTOR suppression and lysosomal decline. Given that chronic
403 mTOR dysregulation, ER stress, and impaired lipid proteostasis are fundamental to
404 diverse pathologies—including metabolic syndrome, neurodegeneration, and
405 malignancy—autolamellasome formation may represent a conserved remodeling
406 response that is either protective or maladaptive depending on the disease context.
407 Future studies integrating unbiased genetic screening, *in vitro* reconstitution, disease
408 modeling, and physiological analyses will be instrumental in defining how
409 autolamellasomes contribute to membrane homeostasis, metabolic resilience, aging,
410 and disease pathogenesis.
411

412 **Figures and figure legends**

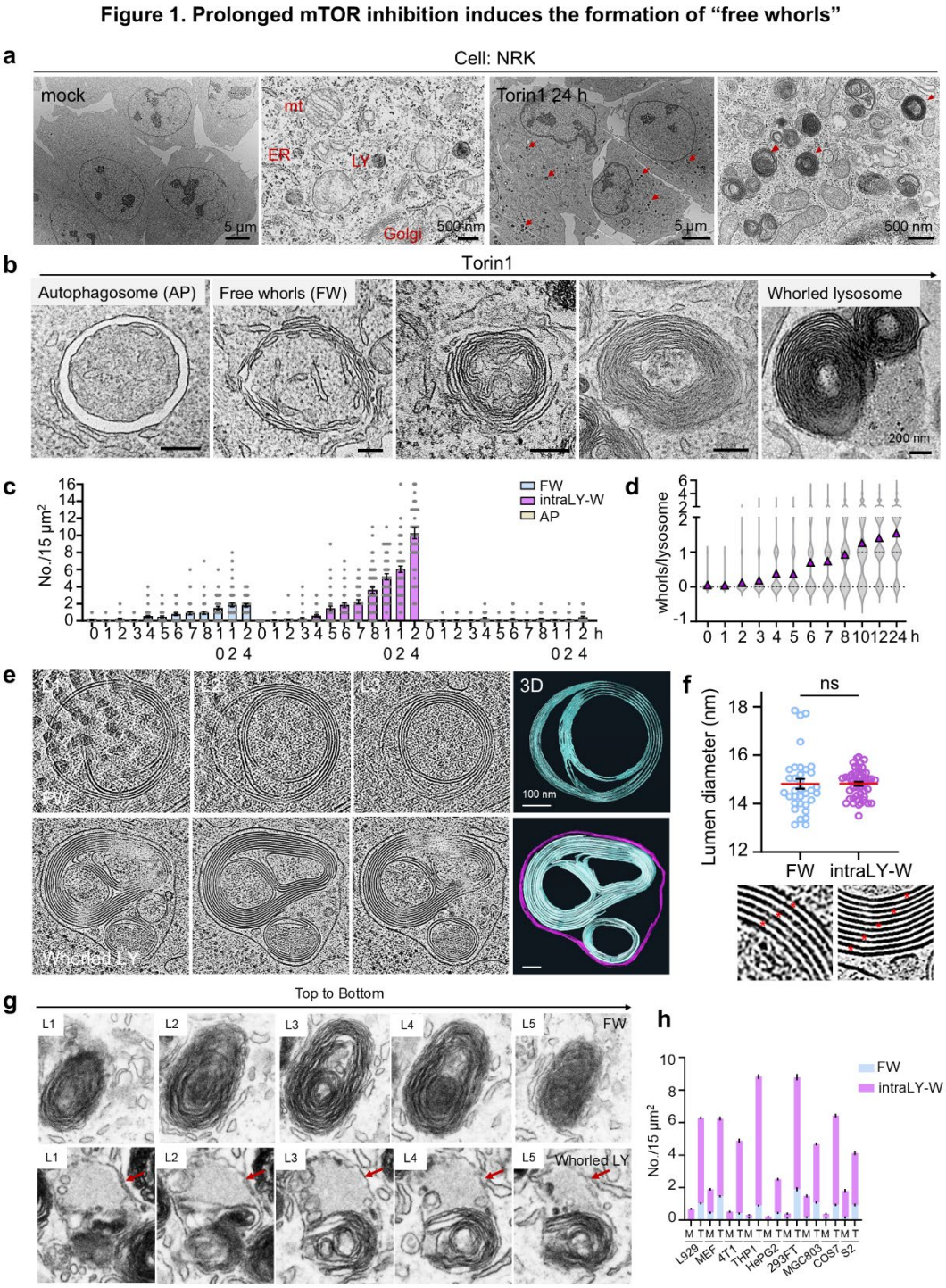

413

414 **Figure 1. Prolonged mTOR inhibition induces the formation of "free whorls".**

415 (a) TEM images of NRK cells ± 1 μM Torin1 (24 h). Red arrows, electron-dense

416 whorls. ER, endoplasmic reticulum; mt, mitochondria; LY, lysosome; Golgi, Golgi

417 apparatus. Scale bars, 5 μm (overview) or 500 nm (magnified).

418 (b) TEM of autophagosomes (AP), free whorls (FW) and lysosomes/autolysosomes
419 containing with whorls (whorled lysosome) in Torin1-treated NRK cells (time series).
420 Scale bars, 200 nm.
421 (c) Quantification of structures (FW, intraLY-W: intralysosomal whorls, AP) from (b)
422 in 15 μm^2 area. n > 38 cells/time point. Data are reported as mean ± SEM.
423 (d) Whorls per lysosome/autolysosome quantified from (b). n > 70 lysosomes/time
424 point. Violin plots show distribution; mean marked by triangles.
425 (e) Cryo-ET (cryo-electron tomography) 3D rendering of FW and whorled lysosome in
426 Torin1-treated (24 h) NRK cells. L1 – L3, structure layers. Scale bars, 100 nm.
427 (f) Lumen diameter quantification from (e). n = 34 (FW), 48 (intraLY-W). ns, not
428 significant; two-tailed unpaired t-test. Asterisks mark lumens. Data are reported as
429 mean ± SEM.
430 (g) Representative FIB (focused ion beam) images of FW and whorled lysosome. L1 –
431 L5, structure layers.
432 (h) FW and intraLY-W quantification from TEM of multiple cell lines (± Torin1, 24
433 h). M, mock; T, Torin1. n values: L929 (M: n=40; T: n=68), MEF (M: n=78; T: n=56),
434 4T1 (M: n=54; T: n=34), THP1 (M: n=43; T: n=46), HepG2 (M: n=74; T: n=54), 293FT
435 (M: n=32; T: n=29), MGC803 (M: n=35; T: n=38), COS7 (M: n=64; T: n=49), and S2
436 (M: n=25; T: n=31).
437

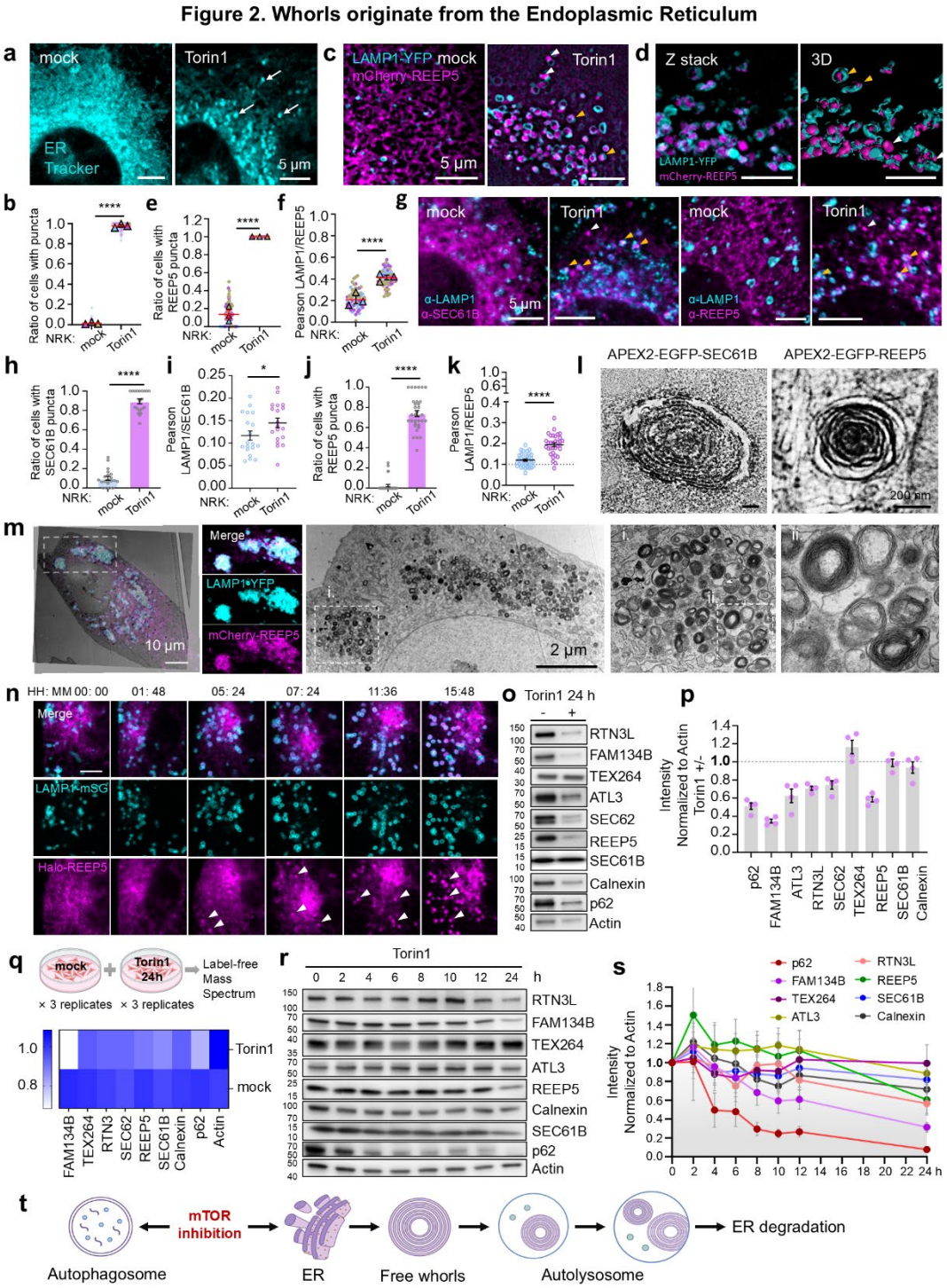

Figure 2. Whorls originate from the Endoplasmic Reticulum.

(a) Representative confocal images of NRK cells ± 1 µM Torin1 (24 h). ER Tracker-labeled. Arrows, ER puncta. Scale bars, 5 µm.

(b) Quantification of cells with ER puncta from (a). n>230 cells/group, 3 experiments. Data are presented as mean ± SEM. ****, p<0.0001 (unpaired t-test).

444 (c) Representative SIM images of NRK cells co-expressing LAMP1-YFP/mCherry-
445 REEP5 ± Torin1 (24 h). White arrows, free-standing ER puncta; yellow arrows, ER
446 puncta inside lysosomes. Scale bars, 5 μm.
447 (d) Representative z-stack and 3D rendering from (c). Scale bars, 5 μm.
448 (e-f) Quantification from (c). (e) Ratio of cells with mCherry-REEP5 labeled-ER
449 puncta. (f) Pearson correlation coefficient of LAMP1-YFP and mCherry-REEP5
450 signals. n>135 cells/group, 3 experiments. Data are presented as mean ± SEM. ****,
451 p<0.0001 (unpaired t-test).
452 (g) Endogenous immunostaining of NRK cells ± Torin1 (24 h). Stained with anti-
453 LAMP1/SEC61B or anti-LAMP1/REEP5. White arrows, free ER puncta; yellow
454 arrows, ER puncta in lysosomes. Scale bars, 5 μm.
455 (h-k) Quantification from (g). (h) Ratio of cells with SEC61B labeled-ER puncta. (i)
456 Pearson correlation coefficient of LAMP1 and SEC61B signals. (j) Ratio of cells with
457 REEP5 labeled-ER puncta. (k) Pearson correlation coefficient of LAMP1 and REEP5
458 signals. n>180 cells/condition. Error bars indicate mean ± SEM. *, p<0.05, ****,
459 p<0.0001 (unpaired t-test).
460 (l) Representative APEX2-TEM images of free whorls in NRK cells stably expressing
461 APEX2-EGFP-SEC61B or APEX2-EGFP-REEP5 treated with Torin1. Scale bar, 200
462 nm.
463 (m) CLEM data of NRK cells stably co-expressing LAMP1-YFP and mCherry-REEP5
464 treated with Torin1. Fluorescent and EM images overlaid; region enlarged (right). Scale
465 bars, 10 μm (overlay) or 2 μm (EM).
466 (n) Time-lapse live cell images of NRK cells stably co-expressing LAMP1-mStaygold
467 and HaloTag-REEP5 treated with Torin1. Snapshots at indicated times. Arrows, ER
468 puncta. Scale bar, 5 μm.
469 (o) Western blot results of NRK cells ± Torin1 (24 h). Cell lysates were subjected to
470 SDS-PAGE and immunoblotted with the indicated antibodies. Blots are representative
471 of n=5 biological replicates.
472 (p) Quantification of integrated band intensities from (o). Individual data points

473 represent relative protein levels in the Torin1-treated group normalized to the untreated
474 control and loading control Actin. n=4 independent biological repeats. Data are
475 presented as mean ± SEM.
476 (q) Heatmap of label-free proteomics of NRK cells ± Torin1 (24 h). Values were
477 median-normalized and expressed as fold change relative to the mock-1 group. n = 3
478 biological replicates. The color scale indicates the magnitude of fold change.
479 (r) Western blot results of NRK cells treated with 1 μM Torin1 in a time series. n=4
480 independent biological replicates.
481 (s) Quantification of integrated band intensities from (r). Individual data points
482 represent relative protein levels in the time point normalized to 0 h and loading control
483 Actin. n=4 independent biological repeats. Data are presented as mean ± SEM.
484 (t) Schematic: mTOR inhibition drives parallel autophagosome and free whorl
485 formation.

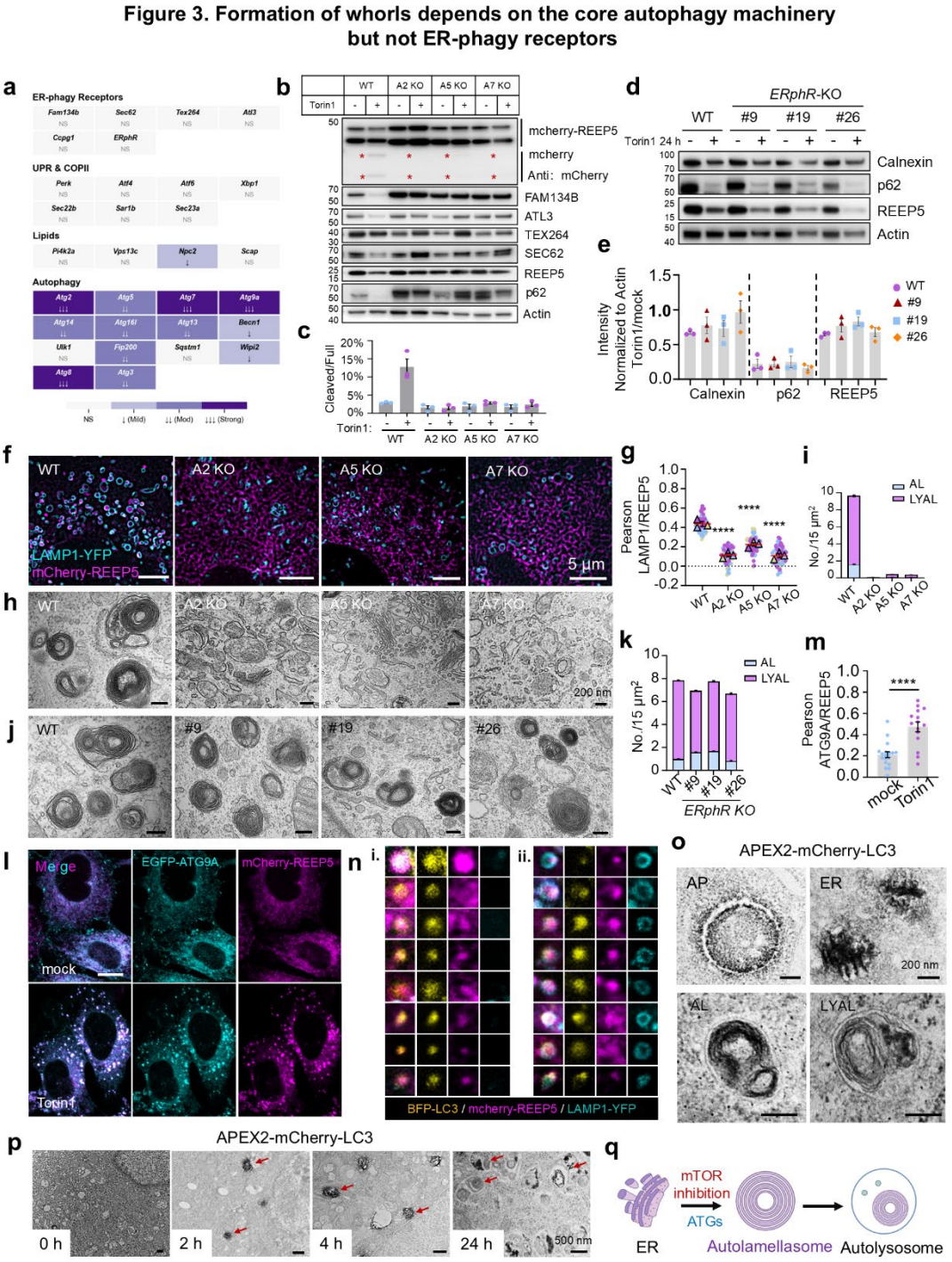

Figure 3. Formation of whorls depends on the core autophagy machinery but not ER-phagy receptors.

(a) Heatmap of knockout genes and their effects on whorls formation. *ERphR*: ER phagy receptor penta KO. ↓ mild，↓↓ moderate, ↓↓↓ strong.

(b) Western blot of endogenous proteins and mCherry cleavage in autophagy-deficient

492 NRK cells (WT, *Atg2/5/7* KO) ± 1 μM Torin1 (24 h). Asterisks, cleaved mCherry
493 fragments; Actin, loading control. n=3 biological replicates.
494 (c) Quantification of mCherry-REEP5 cleavage cleavage from (b). Percentage cleaved
495 fragments relative to full-length. n=3 biological replicates. Data are presented as mean
496 ± SEM.
497 (d) Western blot of *ERphR* KO clones (WT, clones #9, #19, #26) ± 1 μM Torin1 (24
498 h). n=3 biological replicates.
499 (e) Quantification of integrated band intensities from (d). Torin1-treated levels
500 normalized to untreated and Actin. n=3 biological repeats. Data are presented as mean
501 ± SEM.
502 (f) SIM images of WT and autophagy-deficient NRK cells *(Atg2/5/7* KO) co-expressing
503 LAMP1-YFP/mCherry-REEP5, treated with 1 μM Torin1 (24 h). Scale bars, 5 μm.
504 (g) Pearson correlation coefficient (LAMP1/REEP5) from (f). n>300 cells/group, 3
505 experiments. Error bars indicate mean ± SEM. ****, p<0.0001 (unpaired t test).
506 (h) TEM images of WT and autophagy-deficient NRK cells (*Atg2/5/7* KO) treated with
507 1 μM Torin1 (24 h). Scale bars, 200 nm.
508 (i) Quantification from (h): AL (autolamellasome) and LYAL (lysosome/autolysosome
509 with autolamellasome) in 15 μm^2 area. n>37 cells/group. Data are reported as mean ±
510 SEM.
511 (j) Representative TEM images of WT and *ERphR* KO NRK cells treated with 1 μM
512 Torin1 (24 h). Scale bars, 200 nm.
513 (k) Quantification from (j): AL and LYAL in 15 μm^2 area. n>43 cells/group. Data are
514 reported as mean ± SEM.
515 (l) Confocal of NRK cells co-expressing EGFP-ATG9A/mCherry-REEP5 ± 1 μM
516 Torin1 (24 h). Scale bar, 5 μm.
517 (m) Pearson correlation coefficient (ATG9A/REEP5) from (l). n>150 cells/group. Error
518 bars indicate mean ± SEM. ****, p<0.0001 (unpaired t test).
519 (n) Confocal of NRK cells co-expressing BFP-LC3/mCherry-REEP5/LAMP1-YFP
520 (Torin1). (i) BFP-LC3$^+$/mCherry-REEP5$^+$/LAMP1-YFP$^-$ puncta (free ER). (ii)

521 BFP-LC3^{+}/mCherry-REEP5^{+}/LAMP1-YFP^{+} ER puncta (ER in lysosomes).

522 (o) Representative APEX2-TEM images of NRK cells stably expressing APEX2-
523 mCherry-LC3 NRK cells treated with 1 μM Torin1. APEX2 labeled autophagosome
524 (AP), the endoplasmic reticulum (ER), autolamellasome (AL), lysosome/autolysosome
525 containing with autolamellasome (LYAL) are shown as indicated. Scale bars, 200 nm.

526 (p) Time-series APEX2-TEM from (o) (Torin1). Red arrows, LC3^{+} structures. Scale
527 bars, 500 nm.

528 (q) Schematic: ATG genes regulate autolamellasome formation.

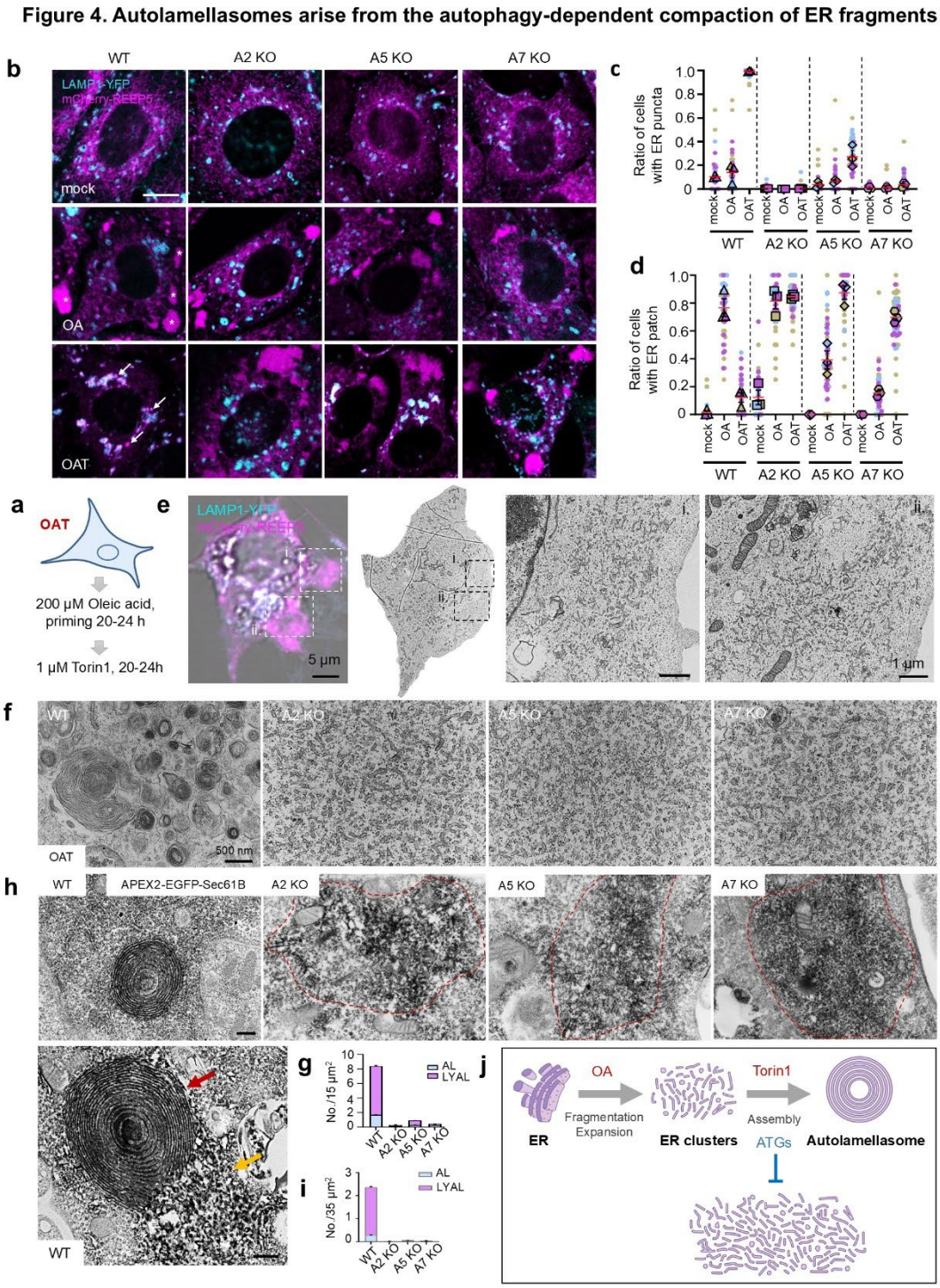

Figure 4. Autolamellasomes arise from the autophagy-dependent compaction of ER fragments.

(a) Schematic of OAT treatment: NRK cells primed with 200 μM oleic acid (OA), then treated with 1 μM Torin1.

(b) Confocal images of WT and autophagy-deficient NRK cells (*Atg2/5/7* KO) co-

535 expressing LAMP1-YFP/mCherry-REEP5, treated with OA or OAT. Arrows, ER
536 puncta; asterisks, ER patches.Scale bar, 5 μm.
537 (c-d) Quantification of cells from (b). (c) Statistics of the ratio of cells with ER puncta.
538 (d) Statistics of the ratio of cells with ER patches. n>70 cells/group, 3 repeats. Error
539 bars indicate mean ± SEM.
540 (e) CLEM data of NRK-*Atg7*-KO cells stably expressing LAMP1-YFP/mCherry-
541 REEP5 treated with OAT. The marked region was enlarged and demonstrated on the
542 right. Scale bars, 5 μm (fluorescence) or 1 μm (EM).
543 (f) Representative TEM images of WT and autophagy-deficient NRK cells treated with
544 OAT. Scale bar, 500 nm.
545 (g) Quantification from (f): AL and LYAL in 15 μm^2 area. n>60 cells/group. Data are
546 reported as mean ± SEM.
547 (h) APEX2-TEM of WT and autophagy-deficient NRK cells expressing APEX2-
548 EGFP-SEC61B (OAT). Red dashed lines, ER fragment clusters; red arrow,
549 autolamellasome; yellow arrow, ER fragments. Scale bars, 500 nm.
550 (i) Quantification from (h): APEX2+ structures (AL: autolamellasome, LYAL:
551 lysosome/autolysosome containing with autolamellasome) in 35 μm^2 area. n>50
552 cells/group. Data are reported as mean ± SEM.
553 (j) Schematic: OA-induced ER fragment clustering and Torin1-driven autophagy-
554 dependent autolamellasome formation.
555

Figure 5. *In vitro* reconstitution of autolamellasome

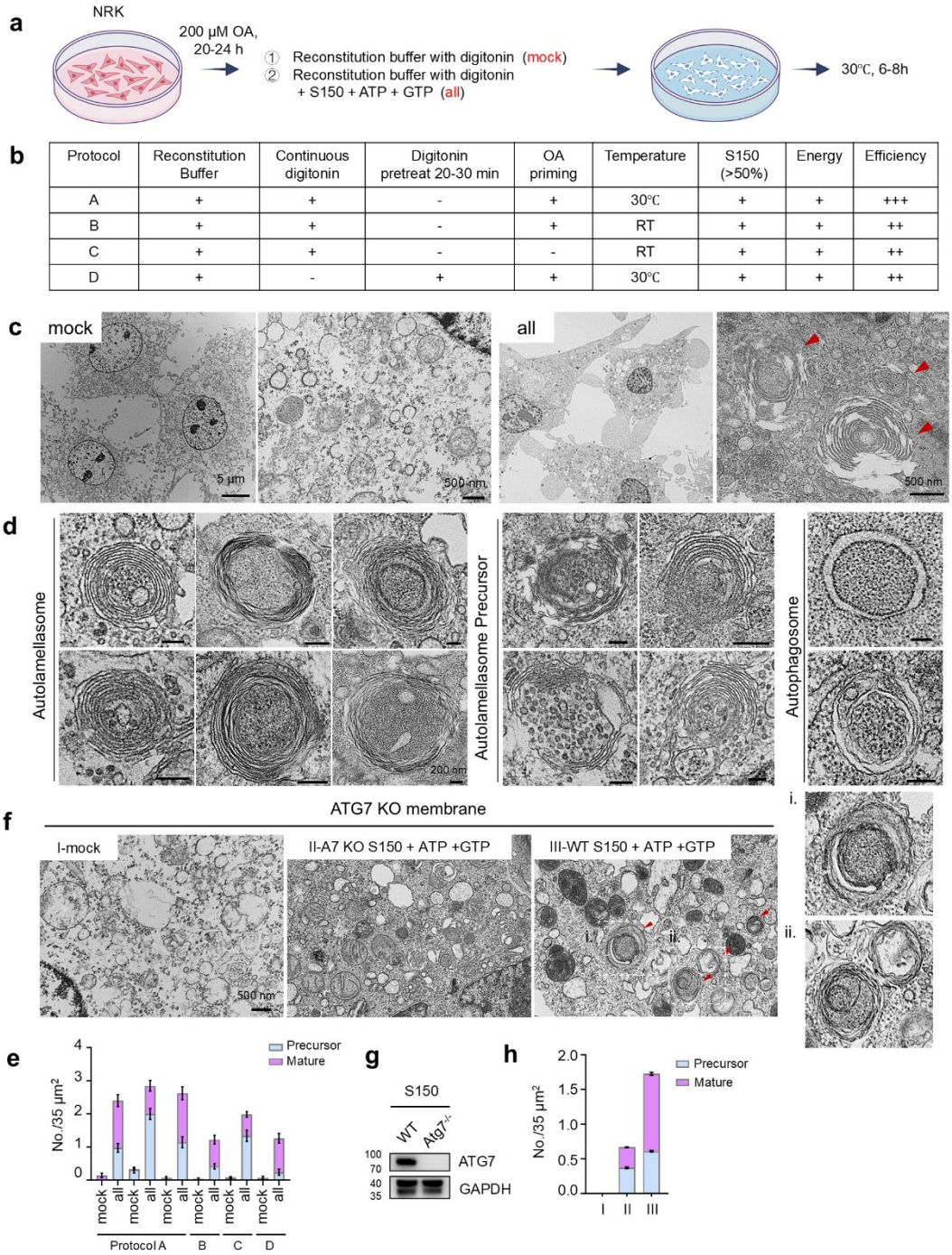

Protocol	Reconstitution Buffer	Continuous digitonin	Digitonin pretreat 20-30 min	OA priming	Temperature	S150 (>50%)	Energy	Efficiency
A	+	+	-	+	30℃	+	+	+++
B	+	+	-	+	RT	+	+	++
C	+	+	-	-	RT	+	+	++
D	+	-	+	+	30℃	+	+	++

Figure 5. *In vitro* reconstitution of autolamellasome.

(a) Schematic of *in vitro* autolamellasome reconstitution. NRK cells primed with 200 μM OA (20-24 h), incubated in buffer ± 40 μg/mL digitonin (mock) or + S150, ATP, GTP (all) for 6-8 h at 30 °C.

(b) Table of various protocols for *in vitro* autolamellasome reconstitution and their

562 efficiencies.

563 (c) TEM of membrane structures (mock vs all, protocol A). Red arrows,
564 autolamellasome-like structures. Scale bars, 5 μm (overview) or 500 nm (magnified).

565 (d) TEM of autolamellasomes, precursors and autophagosomes (all group). Scale bars,
566 200 nm.

567 (e) Quantification of mature autolamellasomes (Mature) and precursors across
568 protocols. Protocol A: n=3 repeats, >35 fields/group. Protocols B-D: >30, >50, >40
569 fields/group respectively. Data are presented as mean ± SEM.

570 (f) Representative TEM images of membrane structures reconstituted with *Atg7*
571 knockout membranes (protocol A). I: buffer + digitonin; II: buffer + *Atg7* KO S150,
572 ATP, GTP; III: buffer + WT S150, ATP, GTP. Red arrows, autolamellasomes. Boxed
573 regions magnified (right). Scale bar, 500 nm.

574 (g) Western blot analysis of S150 from WT and *Atg7* KO NRK cells.

575 (h) Quantification from (f): Mature and precursors. >45 fields/group. Data are presented
576 as mean ± SEM.

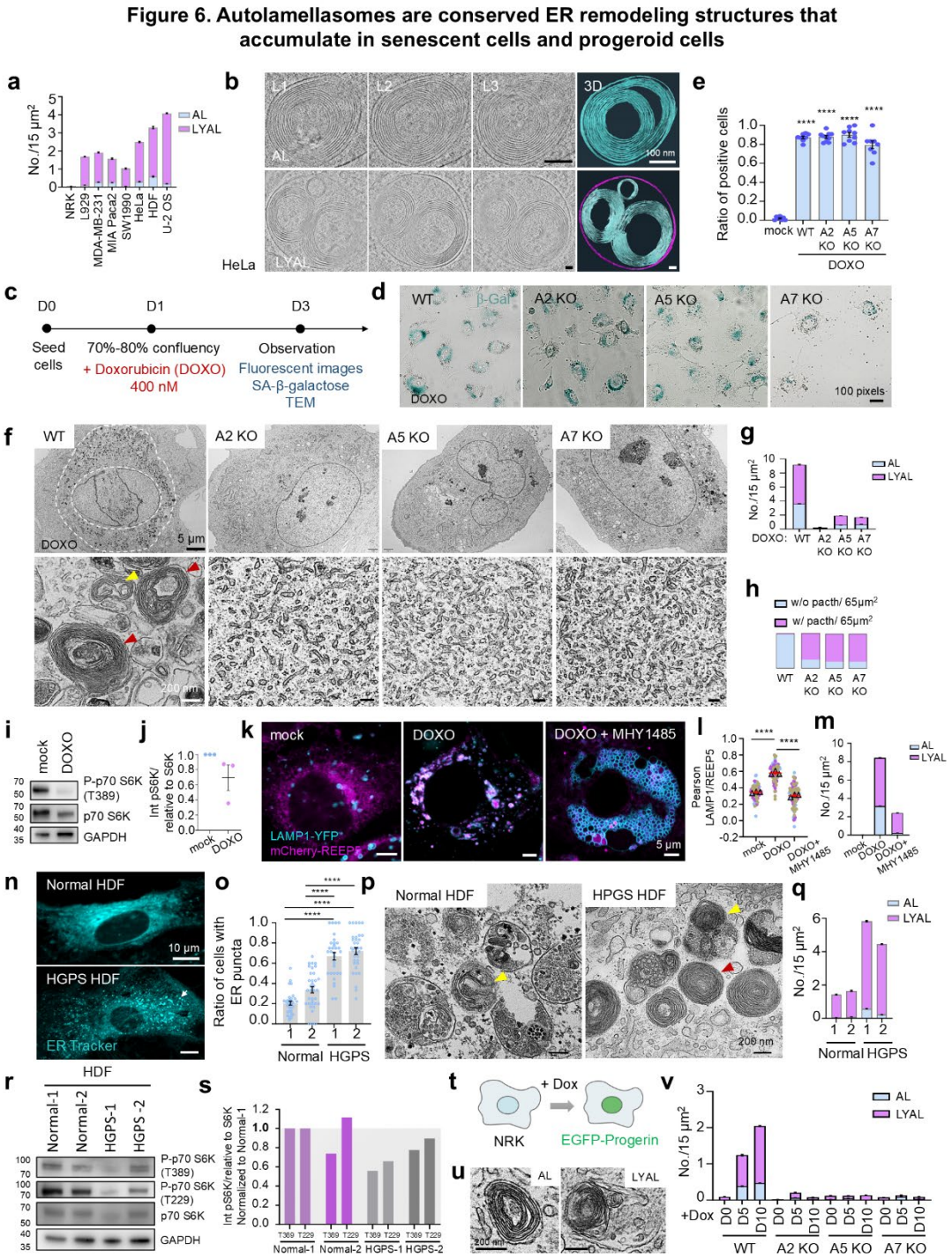

Figure 6. Autolamellasomes are conserved ER remodeling structures that accumulate in senescent cells and progeroid cells.

(a) Quantification of AL and LYAL per 15 μm² area from TEM. n>30 cells/group. Data are reported as mean ± SEM.

(b) Cryo-ET and 3D rendering of AL and LYAL in HeLa cells. L1-L3, structure layers.

583 Scale bars, 100 nm.

584 (c) Schematic: Doxorubicin-induced cellular senescence.

585 (d) β-galactosidase staining of WT and autophagy-deficient NRK cells. Scale bar, 100
586 pixels.

587 (e) Quantification of β-galactosidase-positive cells from (d). n>45 cells/group. Data are
588 presented as mean ± SEM. ****, p<0.0001 (unpaired t test).

589 (f) Representative TEM images of Doxorubicin (DOXO)-treated WT and autophagy-
590 deficient NRK cells. Red arrows, AL; yellow arrow, LYAL. Scale bar, 200 nm.

591 (g) Quantification from (f): AL and LYAL in 15 μm^2 area. n>39 cells/group. Data are
592 reported as mean ± SEM.

593 (h) Quantification of frequency of ER patches per 65 μm^2 area from TEM in (f).

594 (i) Western blot results of NRK cells ± 400 nM DOXO (2 days). n=3 biological
595 replicates. GAPDH served as a loading control.

596 (j) Quantification of phospho-p70 S6K (T389) from (i), normalized to total p70 S6K.
597 n=3 biological repeats. Data are presented as mean ± SEM.

598 (k) Representative confocal images of NRK cells ± 400 nM DOXO, DOXO + 10 μM
599 MHY1485 (2 days).. Scale bars, 5 μm.

600 (l) Pearson correlation coefficient (LAMP1/REEP5) from(k). n>130 cells/group, 3
601 experiments. Data are presented as mean ± SEM. ****, p<0.0001 (unpaired t test).

602 (m) Quantification from TEM: AL and LYAL per 15 μm^2 area (cells treated as in k).
603 n>65 areas/group. Data are reported as mean ± SEM.

604 (n) Representative confocal images of ER Tracker-labeled HDF from normal donors
605 and HGPS patients. Scale bars, 10 μm.

606 (o) Quantification of the ratio of cells with ER puncta from (n). Normal HDF (2 donors)
607 vs HGPS HDF (2 patients). n>225 cells/group. Data are reported as mean ± SEM. ****,
608 p<0.0001 (unpaired t test).

609 (p) TEM of Normal and HGPS HDF. Red arrow, AL; yellow arrows, LYAL. Scale bars,
610 200 nm.

611 (q) Quantification from (p): AL and LYAL in 15 μm^2 area. n>65 areas/group. Data

612 are reported as mean ± SEM.

613 (r) Western blot results of indicated HDF. GAPDH served as a loading control.

614 (s) Phospho-p70 S6K (T389, T229) from (r), normalized to total p70 S6K, relative to

615 Normal-1.

616 (t) Schematic: Doxycycline-inducible EGFP-Progerin in NRK cells.

617 (u) Representative TEM images of AL and LYAL in Dox-induced EGFP-Progerin

618 NRK cells. Scale bars, 200 nm.

619 (v) Quantification from (u): AL and LYAL per 15 μm^2 area. WT and autophagy-

620 deficient NRK cells treated with Dox for 0, 5, 10 days (D0, D5, D10). n>60 areas/group.

621 Data are reported as mean ± SEM.

622

Extended figures and figure legends

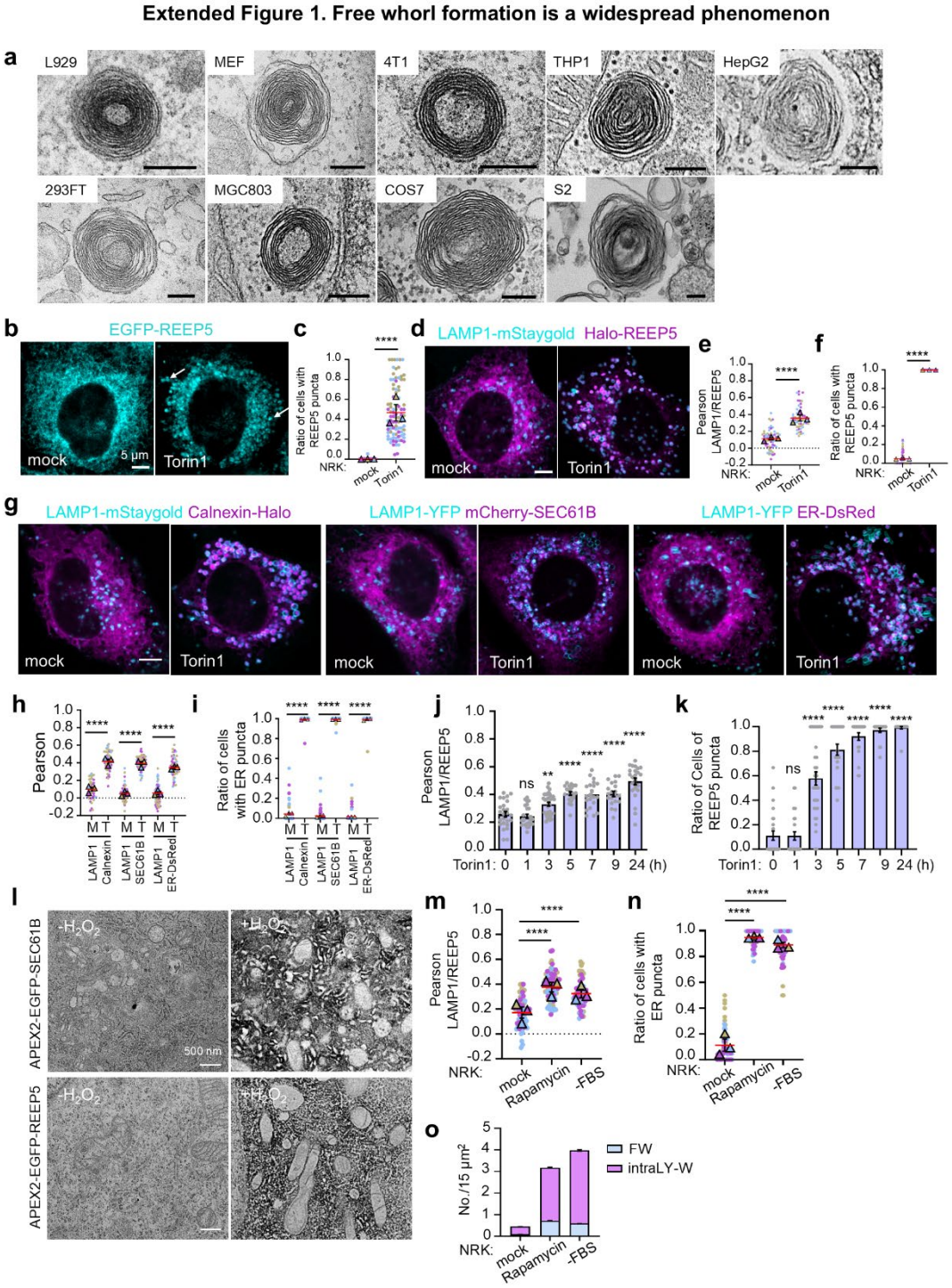

Extended Figure 1. Free whorl formation is a widespread phenomenon.

(a) Representative TEM images of free whorls in various cells treated with 1 μM Torin1 for 24 h. Scale bars, 200 nm.

(b) Representative confocal images of NRK cells expressing EGFP-REEP5 ± Torin1

(24 h). Scale bar, 5 μm.

(c) Quantification of ER puncta-positive cells from (b). n>280 cells/group, 3 experiments. Error bars indicate mean ± SEM. ****, p<0.0001 (unpaired t test).

(d) Representative confocal images of NRK cells expressing LAMP1-mStaygold/HaloTag-REEP5 ± Torin1 (24 h). Scale bar, 5 μm.

(e-f) Quantification from (d). (e) Pearson correlation coefficient (LAMP1-mStaygold/HaloTag-REEP5); (f) Ratio of cells with HaloTag-REEP5 labeled-ER puncta. n>280 cells/group, 3 experiments. Error bars indicate mean ± SEM. ****, p<0.0001(unpaired t test).

(g) Representative confocal images of NRK cells stably expressing LAMP1-mStaygold/Calnexin-HaloTag, LAMP1-YFP/mCherry-SEC61B, LAMP1-YFP/ER-DsRed ± Torin1 (24 h).. Scale bar, 5 μm.

(h-i) Quantification from (g). (h) Pearson correlation coefficient (LAMP1/ER proteins); (i) Ratio of cells with ER puncta. Sample sizes (n) were n>90 (Calnexin), n>100 (SEC61B), n>50 (ER-DsRed). 3 experiments. Error bars indicate mean ± SEM. ****, p<0.0001(unpaired t test).

(j-k) Time series of NRK cells co-expressing LAMP1-YFP/mCherry-REEP5 with Torin1: (j) Pearson correlation coefficient (LAMP1/REEP5); (k) Ratio of cells with ER puncta. n>85 cells/time point. Error bars indicate mean ± SEM. ns, not significant, **, p<0.01, ****, p<0.0001(unpaired t test).

(l) APEX2-TEM images of cells expressing APEX2-EGFP-SEC61B or APEX2-EGFP-REEP5 treated ± H_2O_2. Scale bars, 500 nm.

(m-n) Quantification of NRK cells co-expressing LAMP1-YFP/mCherry-REEP5 treated with 1 μM rapamycin or FBS withdrawal. (m) Pearson correlation coefficient (LAMP1/REEP5); (n) Ratio of cells with ER puncta. n>180 cells/group. Error bars indicate mean ± SEM. ****, p<0.0001(unpaired t test).

(o) TEM of NRK cells treated with rapamycin or serum starvation (24 h). Quantification of FW and intraLY-W in 15 μm^2 area. n>70 cells/group. Data are represented as mean ± SEM.

Extended Figure 2. Autolamellasome formation depends on autophagy core machinery but not ER phagy receptors

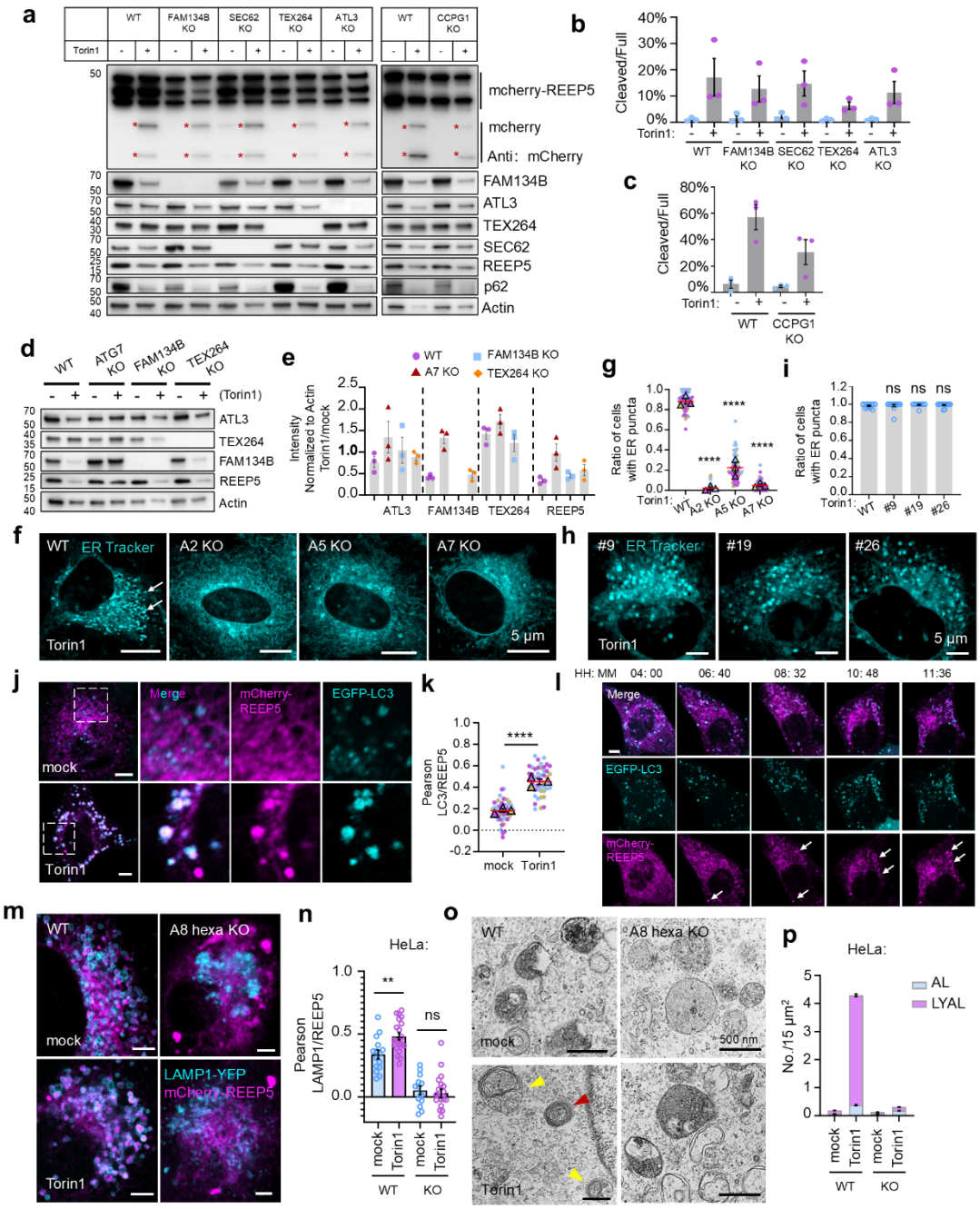

Extended Figure 2. Autolamellasome formation depends on autophagy core machinery but not ER phagy receptors.

(a) Western blot of *ERphR* KO NRK cells (WT, *Fam134b* KO, *Sec62* KO, *Tex264* KO, *Atl3* KO, *Ccpg1* KO) ± 1 μM Torin1 (24 h). Asterisks, cleaved mCherry fragments; Actin, loading control. n=3 biological replicates.

665 (b-c) Quantification of mCherry-REEP5 cleavage(a): (b) Percentage cleaved fragments
666 relative to full-length; (c) Relative intensity of cleaved fragments. n=3 biological
667 replicates. Data are presented as mean ± SEM.
668 (d) Western blot analysis of endogenous proteins in WT, *Atg7* KO, *Fam134b* KO and
669 *Tex264* KO NRK cells ± Torin1 (24 h). Actin, loading control. n=3 biological replicates.
670 (e) Quantification of integrated band intensities from (d). Torin1-treated levels
671 normalized to untreated and Actin. n=3 biological repeats. Data are presented as mean
672 ± SEM.
673 (f) Representative confocal images of WT and autophagy-deficient KO (*Atg2* KO, *Atg5*
674 KO, *Atg7* KO) NRK cells treated with 1 μM Torin1 for 24 h. ER Tracker-labeled.
675 Arrows, ER puncta. Scale bars, 5 μm.
676 (g) Quantification of ER puncta-positive cells from (f). n>250 cells/group, 3
677 experiments. Error bars indicate mean ± SEM. ****, p<0.0001 (unpaired t test).
678 (h) Representative confocal images of *ERphR* KO NRK cells ± Torin1 (24 h), ER
679 Tracker-labeled. Arrows indicate ER puncta. Scale bars, 5 μm.
680 (i) Quantification of the ratio of cells shown in (h) contained with ER puncta. More
681 than 89 cells were analyzed per group. Error bars indicate mean ± SEM. ns, not
682 significant (unpaired t test).
683 (j) Representative confocal images of NRK cells co-expressing EGFP-LC3/mCherry-
684 REEP5 ± Torin1 (24 h). Scale bars, 5 μm.
685 (k) Pearson correlation coefficient (LC3/REEP5) from (j). n>100 cells/group, 3
686 experiments. Error bars indicate mean ± SEM. ****, p<0.0001 (unpaired t test).
687 (l) Time-lapse of NRK cells co-expressing EGFP-LC3/mCherry-REEP5 (Torin1).
688 Snapshots at indicated times. Scale bar, 5 μm.
689 (m) WT and *Atg8* hexa KO HeLa cells co-expressing LAMP1-YFP/mCherry-REEP5 ±
690 Torin1 (24 h). n>30 cells/group. Scale bars, 5 μm.
691 (n) Pearson correlation coefficient (LAMP1/REEP5) from (m). n>30 cells/group. Error
692 bars indicate mean ± SEM. **, p<0.01, ns, not significant (unpaired t test).
693 (o) Representative TEM images of WT and *Atg8* hexa KO HeLa cells ± Torin1 (24 h).

694 Red arrow, AL; yellow arrows, LYAL. Scale bars, 500 nm.

695 (p) Quantification from (o): AL and LYAL in 15 μm² area. n>45 cells/group. Data are

696 reported as mean ± SEM.

Extended Figure 3. Validation of knockout efficiency

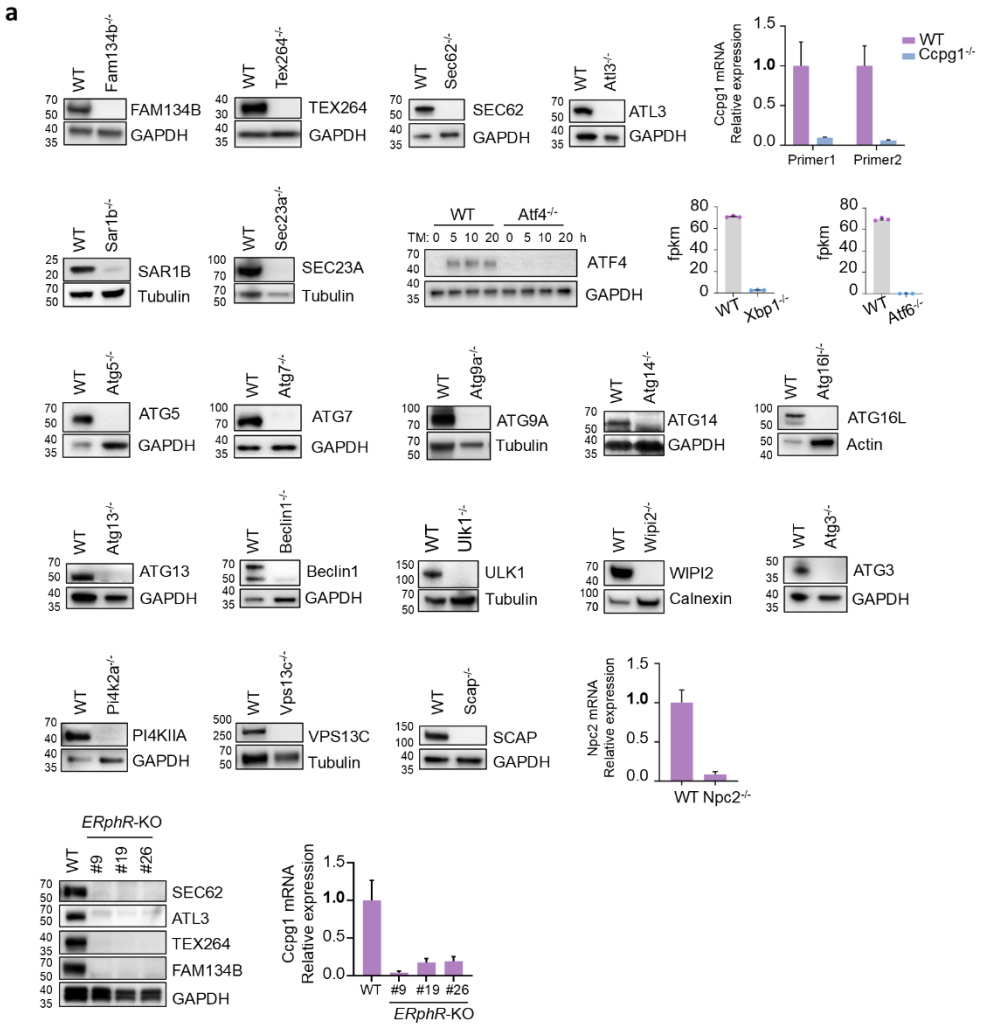

697

698 **Extended Figure 3. Validation of knockout efficiency.**

699 (a) Verification of knockout cells. Western blot results, quantitative RT-PCR and fpkm

700 values are shown here. TM: Tunicamycin.

701

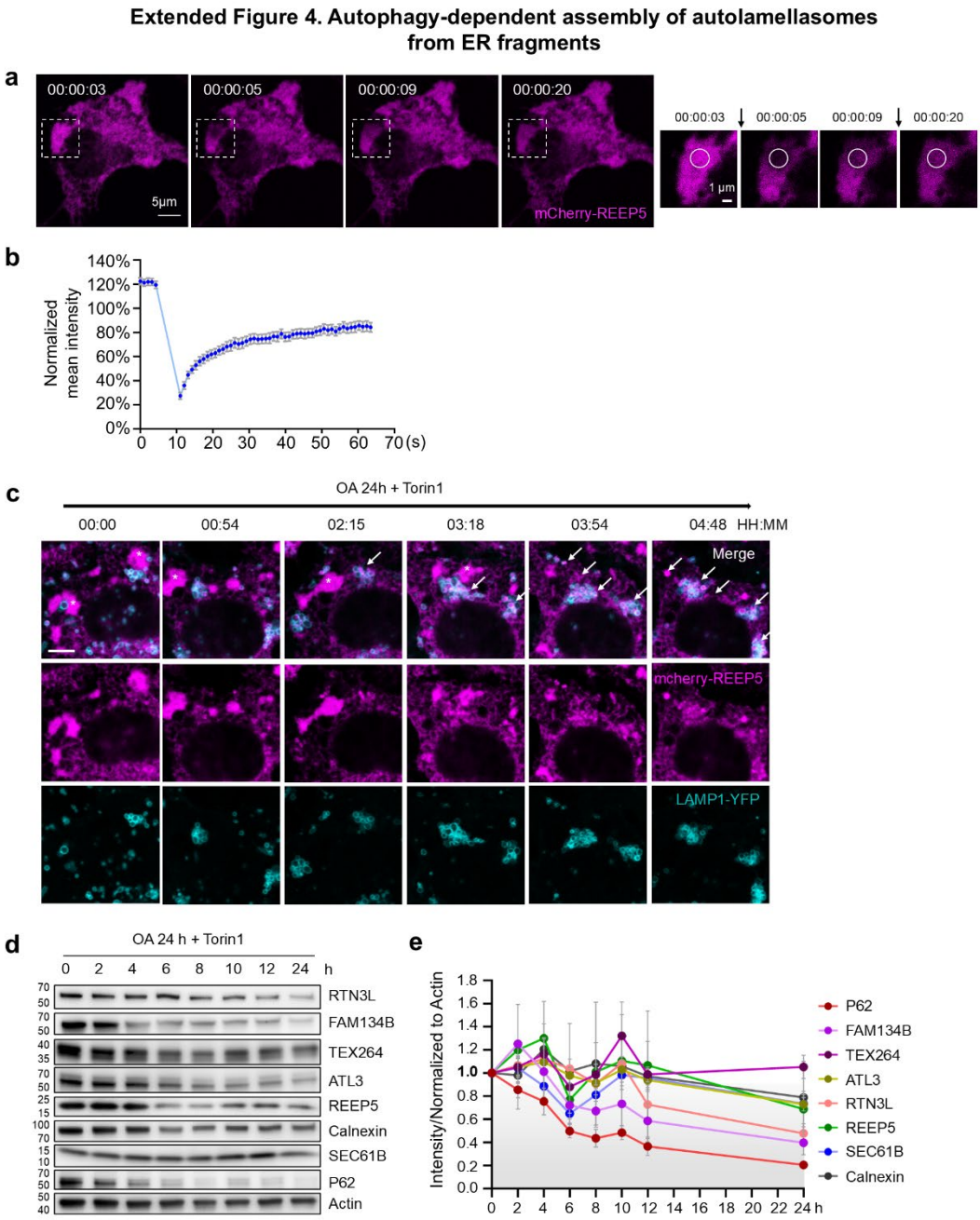

Extended Figure 4. Autophagy-dependent assembly of autolamellasome from ER fragments.

(a) FRAP analysis of OAT-treated NRK-*Atg7*-KO cells expressing mCherry-REEP5. Dashed circles, bleached region. Boxed regions magnified (right). Time relative to bleaching. Scale bars, 5 μm (main), 1 μm (magnified).

(b) Normalized mean fluorescence intensity of bleached region over time. n>20 cells. Data are presented as mean ± SEM. Normalized to pre-bleach.

(c) Time-lapse of NRK cells stably co-expressing LAMP1-YFP/mCherry-REEP5 treated with OAT. Snapshots at indicated times. Arrows, ER puncta; asterisks, ER patches. Scale bar, 5 µm.

(d) Western blot of NRK cells treated with OA (200 µM, 24 h) + Torin1 (1 µM) time series. n=3 biological replicates.

(e) Quantification of integrated band intensities from (d). Protein levels normalized to 0 h and Actin. n=3 biological repeats. Data are presented as mean ± SEM.

Extended Figure 5. *In vitro* reconstitution of autolamellasome

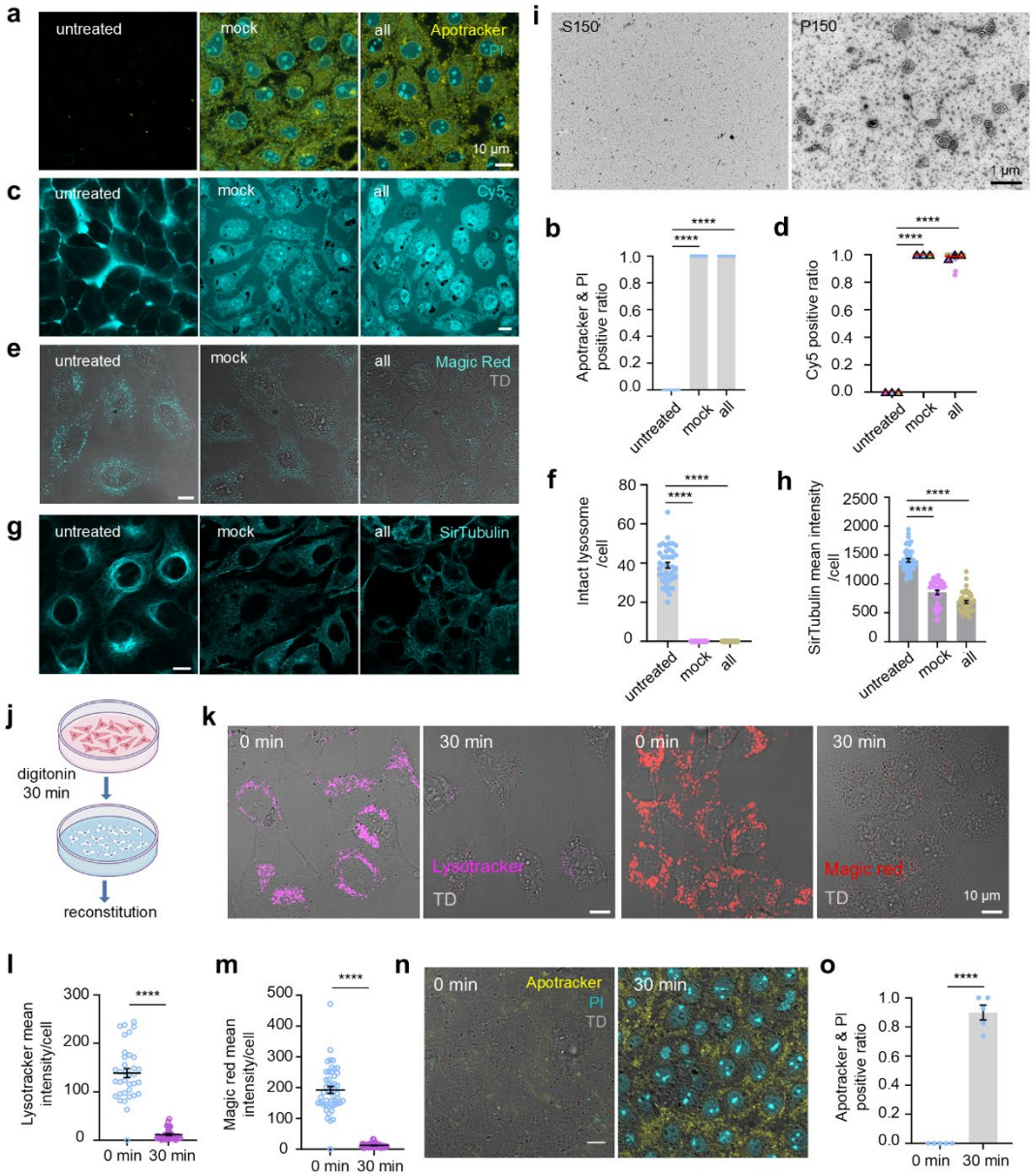

719 **Extended Figure 5. *In vitro* reconstitution of autolamellasome.**

720 (a) Confocal images (protocol A). Cell death verified with Apotracker and propidium
721 iodide (PI). Scale bar, 10 μm.

722 (b) Quantification of Apotracker/PI double-positive cells from (a). n>150 cells. Data
723 are presented as mean ± SEM. ****, p<0.0001 (unpaired t test).

724 (c) Confocal images (protocol A). Cell permeability verified with Cy5. Scale bar, 10
725 μm.

726 (d) Quantification of Cy5-positive cells from (c). n>85 cells/group, 3 experiments. ****,
727 p<0.0001 (unpaired t test).

728 (e) Confocal images (protocol A). Lysosome integrity verified with Magic Red. Scale
729 bar, 10 μm.

730 (f) Quantification of intact lysosomes per cell from (e). n>40 cells. Data are presented
731 as mean ± SEM. ****, p<0.0001 (unpaired t test).

732 (g) Confocal images (protocol A). Microtubule integrity verified with SirTubulin. Scale
733 bar, 10 μm.

734 (h) Quantification of microtubule mean intensity per cell from (g). n>37 cells. Data are
735 presented as mean ± SEM. ****, p<0.0001(unpaired t test).

736 (i) Negative staining-TEM images of S150 and P150. Scale bar, 1 μm.

737 (j) Schematic of Protocol D *in vitro* reconstitution. OA-primed NRK cells
738 permeabilized with 40 μg/mL digitonin (30 min), then incubated in buffer (mock) or
739 buffer + S150, ATP, GTP (all) for 6-8 h at 30 °C.

740 (k) Confocal images (protocol D). NRK cells ± 40 μg/mL digitonin (30 min). Lysosome
741 integrity verified with Lysotracker and Magic Red. Scale bars, 10 μm.

742 (l-m) Quantification of mean intensity: (l) Lysotracker, n>34 cells; (m) Magic Red,
743 n>45 cells. Data are presented as mean ± SEM. ****, p<0.0001(unpaired t test).

744 (n) Cell death (protocol D) verified with Apotracker/PI. Scale bar, 10 μm.

745 (o) Quantification of Apotracker/PI double-positive cells from (n). n>100 cells. Data
746 are presented as mean ± SEM. ****, p<0.0001(unpaired t test).

747

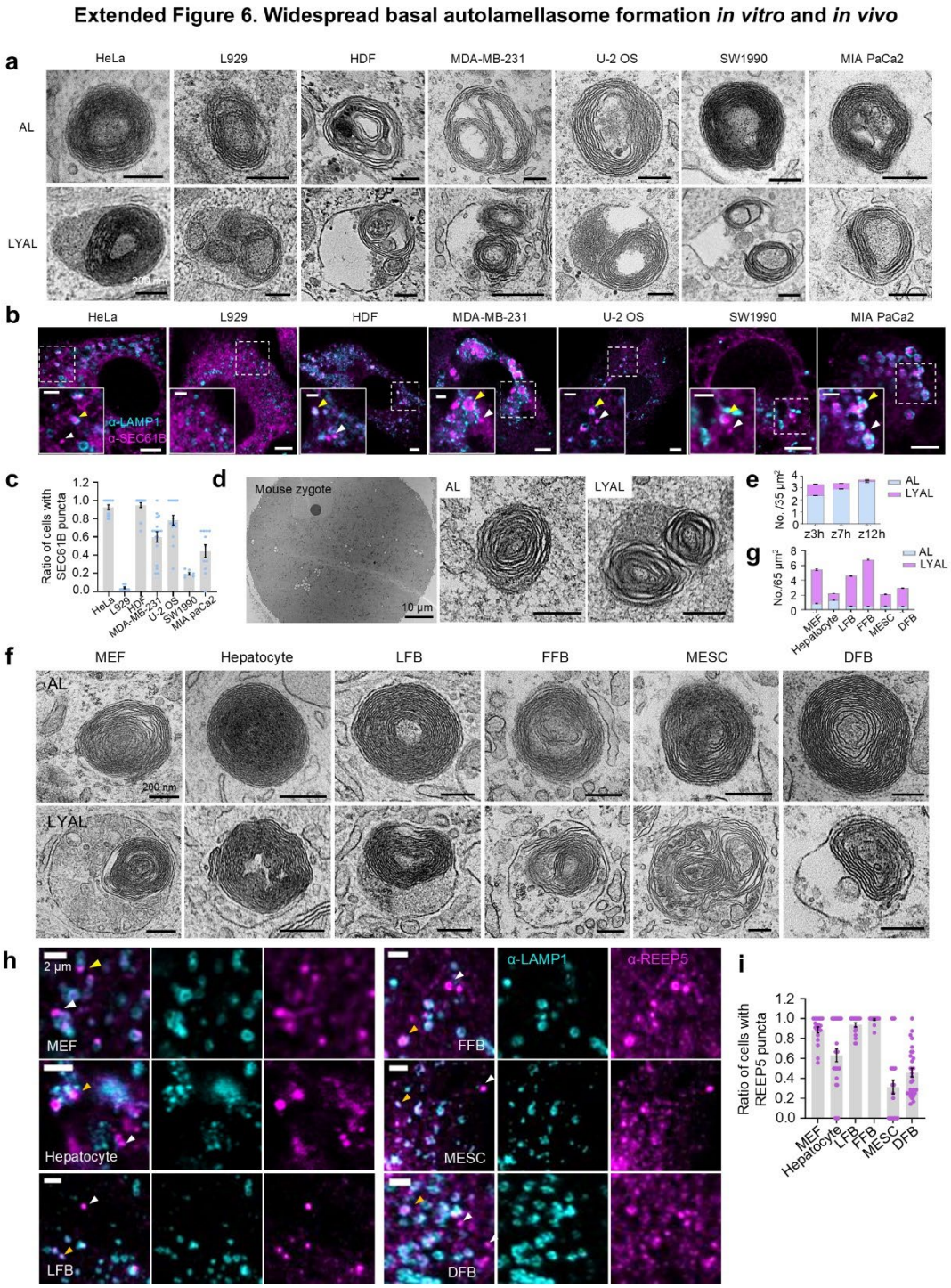

Extended Figure 6. Widespread basal autolamellasome formation *in vitro* and *in vivo*.

(a) Representative TEM images of AL and LYAL in indicated cell lines. Scale bars, 200 nm.

(b) Indicated cell lines were co-stained with anti-LAMP1/ anti-SEC61B. White arrows,

754 free ER puncta; yellow arrows, ER puncta in lysosomes. Scale bars, 5 μm (main), 2 μm
755 (magnified).
756 (c) Statistic of cells from (b) for the ratio of cells with SEC61B puncta. n>38 cells/group.
757 Data are presented as mean ± SEM.
758 (d) Representative TEM images of mouse zygote (whole: scale bar 10 μm) and enlarged
759 view (scale bar 200 nm).
760 (e) Quantification of AL and LYAL per 35 μm^2 from (d) in zygotes collected at 3, 7,
761 12 h. n=3 (z3h, z7h), n=2 (z12h). Data are reported as mean ± SEM.
762 (f) Representative TEM images of AL and LYAL in indicated primary cells. Scale bars,
763 200 nm.
764 (g) Quantification of AL and LYAL per 65 μm^2 from TEM of primary cells. n>35
765 cells/group. Data are reported as mean ± SEM.
766 (h) Indicated primary cells were co-stained with anti-LAMP1/anti-REEP5. White
767 arrows, free ER puncta; yellow arrows, ER puncta in lysosomes. Scale bars, 10 μm
768 (main), 2 μm (magnified).
769 (i) Statistic of cells from (h) for the ratio of cells with REEP5 puncta. n>60 cells/group.
770 Data are presented as mean ± SEM.
771

Extended Figure 7. Autophagy key machinery is essential for basal autolamellasome formation

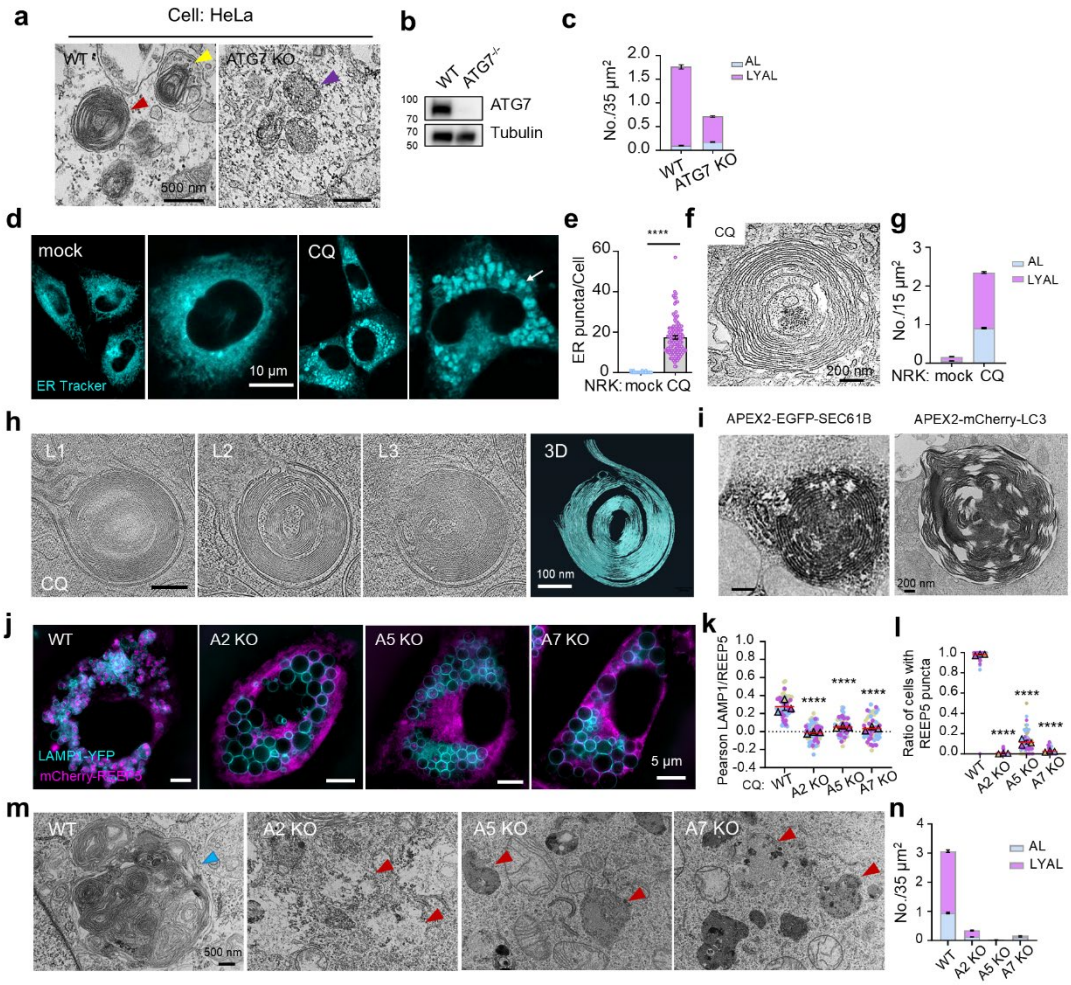

Extended Figure 7. Autophagy key machinery is essential for basal autolamellasome formation.

(a) Representative TEM images of WT and *ATG7* KO HeLa cells. Scale bars, 500 nm.

(b) Western blot validation of ATG7 KO efficiency.

(c) Quantification of AL and LYAL per 35 μm² from (b). n>50 cells/group. Data are reported as mean ± SEM.

(d) Representative confocal images of NRK cells ± 100 nM chloroquine (CQ) for18 h, ER Tracker-labeled. Arrow, ER punctum. Scale bar, 5 μm.

(e) Quantification of ER puncta per cell from (d). n>120 cells. Error bars indicate mean ± SEM. ****, p<0.0001(unpaired t test).

(f) Representative TEM images of NRK cells treated with 100 nM CQ for 18 h. Scale

784 bar, 200 nm.

785 (g) Quantification from (f): AL and LYAL per 15 μm^2 . n>65 cells. Data are reported
786 as mean ± SEM.

787 (h) Cryo-ET and 3D rendering of AL and LYAL in CQ-treated NRK cells (18 h). L1-
788 L3, structure layers. Scale bars, 100 nm.

789 (i) Representative APEX2-TEM images of NRK cells expressing APEX2-EGFP-
790 SEC61B or APEX2-mCherry-LC3, treated with 100 nM CQ for 18 h. Scale bars, 200
791 nm.

792 (j) SIM of WT and autophagy-deficient NRK cells co-expressing LAMP1-
793 YFP/mCherry-REEP5, treated with 100 nM CQ (18 h). Scale bars, 5 µm.

794 (k-l) Quantification from (j): (k) Pearson correlation coefficient (LAMP1/REEP5); (l)
795 Ratio of cells with ER puncta. n>140 cells/group/experiment, 3 experiments. Error bars
796 indicate mean ± SEM. ****, p<0.0001(unpaired t test).

797 (m) Representative TEM images of WT and autophagy-deficient NRK cells (LAMP1-
798 YFP/mCherry-REEP5) treated with 100 nM CQ (18 h). Blue arrow, AL; red arrows,
799 lysosomes. Scale bar, 500 nm.

800 (n) Quantification from (m): AL and LYAL per 35 μm^2 . n>40 cells/group. Data are
801 reported as mean ± SEM.

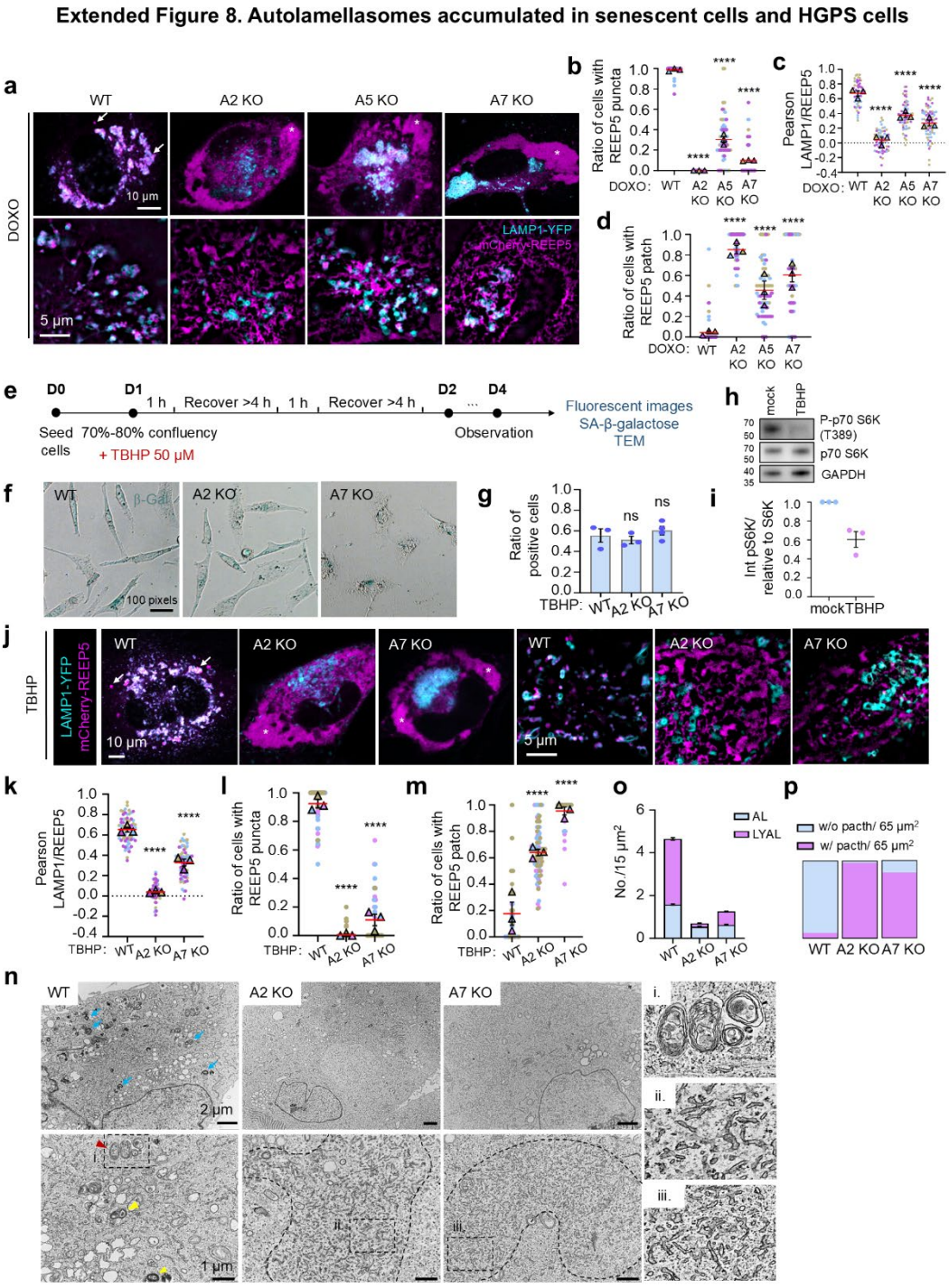

Extended Figure 8. Autolamellasomes accumulated in senescent cells and HGPS cells.

(a) Representative confocal (upper layer) and SIM images (lower layer) of DOXO-treated WT and autophagy-deficient NRK cells. Arrows, ER puncta; asterisks, ER patches. Scale bars, 10 μm (confocal), 5 μm (SIM).

(b-d) Quantification from (a): (b) Ratio of cells with ER puncta. (c) Pearson correlation coefficient (LAMP1/REEP5); (d) Ratio of cells with ER patches. n>49 cells/group, 3 experiments. Data are presented as mean ± SEM. ****, p<0.0001(unpaired t test).

(e) Schematic: TBHP-induced cellular senescence.

(f) β-galactosidase staining of WT and autophagy-deficient NRK cells (*Atg2* KO and *Atg7* KO) after TBHP treatment. *Atg5* KO died shortly after treatment. Scale bar, 100 pixels.

(g) Quantification of β-galactosidase-positive cells from (f). n>40 cells/group. Data are presented as mean ± SEM. ns, not significant (unpaired t test).

(h) Western blot of NRK cells ± TBHP. GAPDH, loading control. n=3 biological replicates.

(i) Quantification of phospho-p70 S6K (T389) from (h), normalized to total p70 S6K. n=3 biological repeats. Data are presented as mean ± SEM.

(j) Confocal (left) and SIM (right) of TBHP-treated WT and autophagy-deficient NRK cells. Arrows, ER puncta; asterisks, ER patches. Scale bars, 10 μm (confocal), 5 μm (SIM).

(k-m) Quantification from (j): (k) Pearson correlation coefficient (LAMP1/REEP5); (l) Ratio of cells with ER puncta; (m) Ratio of cells with ER patches. n>65 cells/group, 3 experiments. Data are presented as mean ± SEM. ****, p<0.0001(unpaired t test).

(n) Representative TEM images of TBHP-treated WT and autophagy-deficient NRK cells. Blue arrows, electron-dense structures; red arrows, AL; yellow arrow, LYAL; black dashed lines, ER fragment clusters. Boxed regions magnified (right). Scale bars, 2 μm (upper), 1 μm (lower).

(o) Quantification from (n): AL and LYAL in 15 μm^2 area. n>40 cells/group. Data are reported as mean ± SEM.

(p) Frequency of ER patch per 65 μm^2 area from TEM images in (n).

Extended Figure 9. Progerin drives autolamellasome accumulation

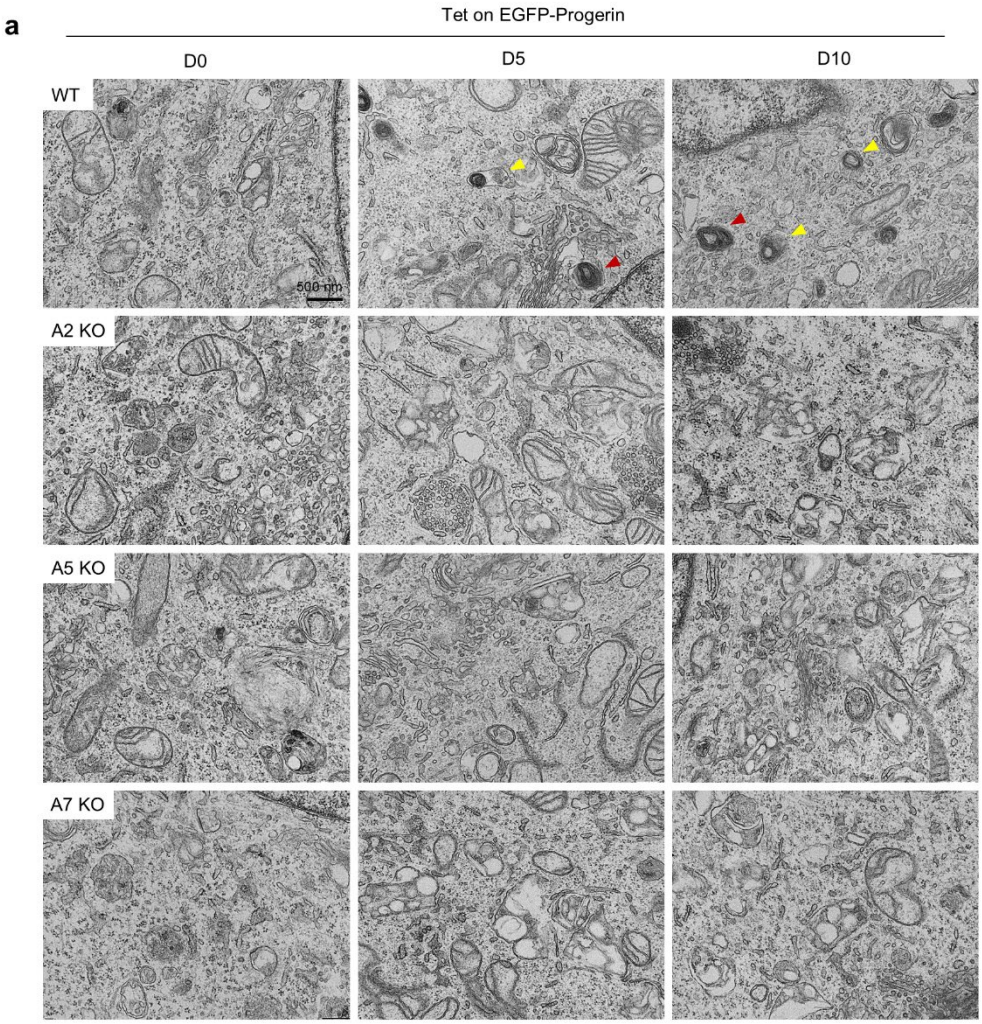

Extended Figure 9. Progerin drives autolamellasome formation.

(a) Representative TEM images of WT and autophagy-deficient NRK cells expressing doxycycline-inducible EGFP-Progerin, induced for 0, 5, or 10 days (D0, D5, D10). Red arrows, AL; yellow arrow, LYAL. Scale bars, 500 nm.

Supplementary videos and information

Supplementary video 1. Continuous formation of ER puncta and their translocation into lysosomes/autolysosomes during Torin1 treatment. Time-lapse live cell imaging of NRK cells stably co-expressing LAMP1-mStaygold and HaloTag-REEP5 treated with 1 μM Torin1**.** Cells were imaged under Olympus FV4000 confocal

847 microscope**.** Scale bar, 10 μm.

848

849 **Supplementary video 2. Continuous formation of ER puncta and their**
850 **colocalization with LC3 during Torin1 treatment.** Time-lapse live cell imaging of
851 NRK cells stably co-expressing BFP-LC3 and mCherry-REEP5 treated with 1 μM
852 Torin1 starting at 4 h and imaged on an Olympus FV4000 confocal microscope**.** Scale
853 bar, 10 μm.

854

855 **Supplementary video 3. FRAP analysis of ER patch.** *Atg7* KO NRK cells stably
856 expressing mCherry-REEP5 were primed with 200 μM oleic acid for 24 h, then treated
857 with 1 μM Torin1 for 20 h. Cells were photobleached and imaged on a Nikon AX R
858 microscope. Scale bar, 10 μm.

859

860 **Supplementary video 4. Continuous transition from ER patches to ER puncta**
861 **during Torin1 treatment.** Time-lapse live cell imaging of NRK cells stably co-
862 expressing Lamp1-YFP and mCherry-REEP5. Cells were pretreated with 200 μM oleic
863 acid for 24 h, then treated with 1 μM Torin1 and imaged on an Olympus FV4000
864 confocal microscope. Scale bar, 10 μm.

865

866 **References**

867 1 Tsukada, M. & Ohsumi, Y. Isolation and characterization of autophagy-defective mutants
868 of Saccharomyces cerevisiae. *FEBS Lett* **333**, 169-174 (1993).
869 https://doi.org:10.1016/0014-5793(93)80398-e
870 2 Takeshige, K., Baba, M., Tsuboi, S., Noda, T. & Ohsumi, Y. Autophagy in yeast
871 demonstrated with proteinase-deficient mutants and conditions for its induction. *J Cell*
872 *Biol* **119**, 301-311 (1992). https://doi.org:10.1083/jcb.119.2.301
873 3 Mizushima, N. *et al.* A protein conjugation system essential for autophagy. *Nature* **395**,
874 395-398 (1998). https://doi.org:10.1038/26506
875 4 Kametaka, S., Matsuura, A., Wada, Y. & Ohsumi, Y. Structural and functional analyses of
876 APG5, a gene involved in autophagy in yeast. *Gene* **178**, 139-143 (1996).
877 https://doi.org:10.1016/0378-1119(96)00354-x
878 5 Deretic, V. & Klionsky, D. J. How cells clean house. *Sci Am* **298**, 74-81 (2008).
879 https://doi.org:10.1038/scientificamerican0508-74
880 6 Nishimura, T. & Tooze, S. A. Emerging roles of ATG proteins and membrane lipids in

881 autophagosome formation. *Cell Discov* **6**, 32 (2020). https://doi.org:10.1038/s41421-020-
882 0161-3
883 7 Gómez-Sánchez, R., Tooze, S. A. & Reggiori, F. Membrane supply and remodeling during
884 autophagosome biogenesis. *Curr Opin Cell Biol* **71**, 112-119 (2021).
885 https://doi.org:10.1016/j.ceb.2021.02.001
886 8 Vargas, J. N. S., Hamasaki, M., Kawabata, T., Youle, R. J. & Yoshimori, T. The mechanisms
887 and roles of selective autophagy in mammals. *Nat Rev Mol Cell Biol* **24**, 167-185 (2023).
888 https://doi.org:10.1038/s41580-022-00542-2
889 9 Li, W. *et al.* Selective autophagy of intracellular organelles: recent research advances.
890 *Theranostics* **11**, 222-256 (2021). https://doi.org:10.7150/thno.49860
891 10 Pankiv, S. *et al.* p62/SQSTM1 binds directly to Atg8/LC3 to facilitate degradation of
892 ubiquitinated protein aggregates by autophagy. *J Biol Chem* **282**, 24131-24145 (2007).
893 https://doi.org:10.1074/jbc.M702824200
894 11 Birgisdottir Å, B., Lamark, T. & Johansen, T. The LIR motif - crucial for selective autophagy.
895 *J Cell Sci* **126**, 3237-3247 (2013). https://doi.org:10.1242/jcs.126128
896 12 Grumati, P., Dikic, I. & Stolz, A. ER-phagy at a glance. *J Cell Sci* **131** (2018).
897 https://doi.org:10.1242/jcs.217364
898 13 Bravo, R. *et al.* Endoplasmic reticulum and the unfolded protein response: dynamics and
899 metabolic integration. *Int Rev Cell Mol Biol* **301**, 215-290 (2013).
900 https://doi.org:10.1016/b978-0-12-407704-1.00005-1
901 14 Schwarz, D. S. & Blower, M. D. The endoplasmic reticulum: structure, function and
902 response to cellular signaling. *Cell Mol Life Sci* **73**, 79-94 (2016).
903 https://doi.org:10.1007/s00018-015-2052-6
904 15 Stolz, A. & Grumati, P. The various shades of ER-phagy. *Febs j* **286**, 4642-4649 (2019).
905 https://doi.org:10.1111/febs.15031
906 16 Schuck, S., Gallagher, C. M. & Walter, P. ER-phagy mediates selective degradation of
907 endoplasmic reticulum independently of the core autophagy machinery. *J Cell Sci* **127**,
908 4078-4088 (2014). https://doi.org:10.1242/jcs.154716
909 17 Fregno, I. & Molinari, M. Proteasomal and lysosomal clearance of faulty secretory proteins:
910 ER-associated degradation (ERAD) and ER-to-lysosome-associated degradation (ERLAD)
911 pathways. *Crit Rev Biochem Mol Biol* **54**, 153-163 (2019).
912 https://doi.org:10.1080/10409238.2019.1610351
913 18 Khaminets, A. *et al.* Regulation of endoplasmic reticulum turnover by selective autophagy.
914 *Nature* **522**, 354-358 (2015). https://doi.org:10.1038/nature14498
915 19 Grumati, P. *et al.* Full length RTN3 regulates turnover of tubular endoplasmic reticulum
916 via selective autophagy. *Elife* **6** (2017). https://doi.org:10.7554/eLife.25555
917 20 Rudinskiy, M., Galli, C., Raimondi, A. & Molinari, M. The intrinsically disordered regions of
918 organellophagy receptors are interchangeable and control organelle fragmentation, ER-
919 phagy and mitophagy flux. *Nat Cell Biol* **27**, 1431-1447 (2025).
920 https://doi.org:10.1038/s41556-025-01728-4
921 21 Chen, Q. *et al.* ATL3 Is a Tubular ER-Phagy Receptor for GABARAP-Mediated Selective
922 Autophagy. *Curr Biol* **29**, 846-855.e846 (2019). https://doi.org:10.1016/j.cub.2019.01.041
923 22 Mochida, K. & Nakatogawa, H. ER-phagy: selective autophagy of the endoplasmic
924 reticulum. *EMBO Rep* **23**, e55192 (2022). https://doi.org:10.15252/embr.202255192

23 Smith, M. D. *et al.* CCPG1 Is a Non-canonical Autophagy Cargo Receptor Essential for ER-Phagy and Pancreatic ER Proteostasis. *Dev Cell* **44**, 217-232.e211 (2018). https://doi.org:10.1016/j.devcel.2017.11.024

24 Pollard, T. D., Earnshaw, W. C., Lippincott-Schwartz, J., and Johnson, G. T. . *Cell Biology: Third Edition.*, (Elsevier, 2016).

25 Klumperman, J. & Raposo, G. The complex ultrastructure of the endolysosomal system. *Cold Spring Harb Perspect Biol* **6**, a016857 (2014). https://doi.org:10.1101/cshperspect.a016857

26 Germain, D. P. Fabry disease. *Orphanet J Rare Dis* **5**, 30 (2010). https://doi.org:10.1186/1750-1172-5-30

27 Wu, S. Z. *et al.* Hydroxychloroquine-induced renal phospholipidosis resembling Fabry disease in undifferentiated connective tissue disease: A case report. *World J Clin Cases* **7**, 4377-4383 (2019). https://doi.org:10.12998/wjcc.v7.i24.4377

28 Raposo, G., Marks, M. S. & Cutler, D. F. Lysosome-related organelles: driving post-Golgi compartments into specialisation. *Curr Opin Cell Biol* **19**, 394-401 (2007). https://doi.org:10.1016/j.ceb.2007.05.001

29 Faigle, W. *et al.* Deficient peptide loading and MHC class II endosomal sorting in a human genetic immunodeficiency disease: the Chediak-Higashi syndrome. *J Cell Biol* **141**, 1121-1134 (1998). https://doi.org:10.1083/jcb.141.5.1121

30 Platt, F. M., Boland, B. & van der Spoel, A. C. The cell biology of disease: lysosomal storage disorders: the cellular impact of lysosomal dysfunction. *J Cell Biol* **199**, 723-734 (2012). https://doi.org:10.1083/jcb.201208152

31 Xu, F. *et al.* COPII mitigates ER stress by promoting formation of ER whorls. *Cell Res* **31**, 141-156 (2021). https://doi.org:10.1038/s41422-020-00416-2

32 Fumagalli, F. *et al.* Translocon component Sec62 acts in endoplasmic reticulum turnover during stress recovery. *Nat Cell Biol* **18**, 1173-1184 (2016). https://doi.org:10.1038/ncb3423

33 Chino, H., Hatta, T., Natsume, T. & Mizushima, N. Intrinsically Disordered Protein TEX264 Mediates ER-phagy. *Mol Cell* **74**, 909-921.e906 (2019). https://doi.org:10.1016/j.molcel.2019.03.033

34 An, H. *et al.* TEX264 Is an Endoplasmic Reticulum-Resident ATG8-Interacting Protein Critical for ER Remodeling during Nutrient Stress. *Mol Cell* **74**, 891-908.e810 (2019). https://doi.org:10.1016/j.molcel.2019.03.034

35 Orsi, A. *et al.* Dynamic and transient interactions of Atg9 with autophagosomes, but not membrane integration, are required for autophagy. *Mol Biol Cell* **23**, 1860-1873 (2012). https://doi.org:10.1091/mbc.E11-09-0746

36 Judith, D. & Tooze, S. A. ATG9A supplies PtdIns4P to the autophagosome initiation site. *Autophagy* **15**, 1660-1661 (2019). https://doi.org:10.1080/15548627.2019.1632124

37 Chen, F. *et al.* FIT2 organizes lipid droplet biogenesis with ER tubule-forming proteins and septins. *J Cell Biol* **220** (2021). https://doi.org:10.1083/jcb.201907183

38 Ruohola, H., Kabcenell, A. K. & Ferro-Novick, S. Reconstitution of transport from the ER to the Golgi complex in yeast using microsomes and permeabilized yeast cells. *Methods Cell Biol* **31**, 143-154 (1989). https://doi.org:10.1016/s0091-679x(08)61606-4

39 Baker, D., Hicke, L., Rexach, M., Schleyer, M. & Schekman, R. Reconstitution of SEC gene

product-dependent intercompartmental protein transport. *Cell* **54**, 335-344 (1988). https://doi.org:10.1016/0092-8674(88)90196-1

40 Chang, B. D. *et al.* Role of p53 and p21waf1/cip1 in senescence-like terminal proliferation arrest induced in human tumor cells by chemotherapeutic drugs. *Oncogene* **18**, 4808-4818 (1999). https://doi.org:10.1038/sj.onc.1203078

41 Chen, Q. & Ames, B. N. Senescence-like growth arrest induced by hydrogen peroxide in human diploid fibroblast F65 cells. *Proc Natl Acad Sci U S A* **91**, 4130-4134 (1994). https://doi.org:10.1073/pnas.91.10.4130

42 López-Otín, C., Blasco, M. A., Partridge, L., Serrano, M. & Kroemer, G. Hallmarks of aging: An expanding universe. *Cell* **186**, 243-278 (2023). https://doi.org:10.1016/j.cell.2022.11.001

43 Sun, D., Wu, R., Zheng, J., Li, P. & Yu, L. Polyubiquitin chain-induced p62 phase separation drives autophagic cargo segregation. *Cell Res* **28**, 405-415 (2018). https://doi.org:10.1038/s41422-018-0017-7

44 Sho, T., Li, Y., Jiao, H. & Yu, L. Migratory autolysosome disposal mitigates lysosome damage. *J Cell Biol* **223** (2024). https://doi.org:10.1083/jcb.202403195

45 Nguyen, T. N. *et al.* Atg8 family LC3/GABARAP proteins are crucial for autophagosome-lysosome fusion but not autophagosome formation during PINK1/Parkin mitophagy and starvation. *J Cell Biol* **215**, 857-874 (2016). https://doi.org:10.1083/jcb.201607039

46 Ren, J. *et al.* Multi-site-mediated entwining of the linear WIR-motif around WIPI β-propellers for autophagy. *Nat Commun* **11**, 2702 (2020). https://doi.org:10.1038/s41467-020-16523-y

47 Wagner, F. R. *et al.* Preparing samples from whole cells using focused-ion-beam milling for cryo-electron tomography. *Nat Protoc* **15**, 2041-2070 (2020). https://doi.org:10.1038/s41596-020-0320-x

48 Zheng, S. Q. *et al.* MotionCor2: anisotropic correction of beam-induced motion for improved cryo-electron microscopy. *Nat Methods* **14**, 331-332 (2017). https://doi.org:10.1038/nmeth.4193

49 Mastronarde, D. N. & Held, S. R. Automated tilt series alignment and tomographic reconstruction in IMOD. *J Struct Biol* **197**, 102-113 (2017). https://doi.org:10.1016/j.jsb.2016.07.011

50 Edelman, B. L. & Redente, E. F. Isolation and Characterization of Mouse Fibroblasts. *Methods Mol Biol* **1809**, 59-67 (2018). https://doi.org:10.1007/978-1-4939-8570-8_5

51 Correa-Gallegos, D. *et al.* CD201(+) fascia progenitors choreograph injury repair. *Nature* **623**, 792-802 (2023). https://doi.org:10.1038/s41586-023-06725-x

52 Xu, Z. *et al.* Anatomically distinct fibroblast subsets determine skin autoimmune patterns. *Nature* **601**, 118-124 (2022). https://doi.org:10.1038/s41586-021-04221-8

53 Charni-Natan, M. & Goldstein, I. Protocol for Primary Mouse Hepatocyte Isolation. *STAR Protoc* **1**, 100086 (2020). https://doi.org:10.1016/j.xpro.2020.100086

54 Rizo, J. A., Spencer, T. E. & Kelleher, A. M. Protocol for the establishment and characterization of an endometrial-derived epithelial organoid and stromal cell co-culture system. *STAR Protoc* **5**, 102894 (2024). https://doi.org:10.1016/j.xpro.2024.102894

55 Wang, X. *et al.* Nuclear envelope budding inhibition slows down progerin-induced aging process. *Proc Natl Acad Sci U S A* **121**, e2321378121 (2024).

https://doi.org:10.1073/pnas.2321378121

Resource availability

Further information and requests for resources and reagents should be directed to and will be fulfilled by the lead contact, Li Yu. All data supporting the findings of this study are available from the corresponding author upon reasonable request.

Materials and Methods

All research adhered to the guidelines from the Academic Integrity and Ethics committee of Tsinghua University.

Reagents

Torin1 (MCE, HY-13003), ER-Tracker™ Blue-White DPX (ThermoFisher, E12353), 3,3′-Diaminobenzidine tetrahydrochloride hydrate (DAB tetrahydrochloride hydrate, Sigma-Aldrich, D5637), Hydrogen peroxide (Sigma-Aldrich, 88597), Rapamycin (MCE, HY-10219), Sodium oleate (Sigma-Aldrich, O7501), Chloroquine (MCE, HY-17589A); ATP (ThermoFisher, R0441); GTP (Sangon Biotech, A620332-0250); Creatine Phosphate 2Na (Lablead, 0271); Creatine Kinase (Yeasen, 14502ES10); Apotracker Green (BioLegend, 427401); Propidium iodide Staining Solution (Yeasen, 40710ES03); Cy5 (Solarbio, S1053); Lysotracker (Invitrogen, L12492); Magic Red (Abcam, ab270772)); SirTubulin (Cytoskeleton, Inc., CY-SC002); Doxorubicin hydrochloride (MCE, HY-15142); TBHP (tert-Butyl hydroperoxide solution, Aladdin, B106035), G418 sulfate (Amresco, E859), Hygromycin B (Roche, 10843555001), Puromycin (ThermoFisher, A1113803), Doxycycline (Sigma-Aldrich, D3072), Vigofect (Vigorous, T001), Senescence β-Galactosidase Staining Kit (Beyotime, C0602), Collagenase I (Solarbio, C8140), Collagenase IV (Yeasen, 40510ES76), DNaseI (Aladdin, D106200), Liberase (Sigma-Aldrich, 05401127001).

Antibodies

RTN3 (Proteintech Cat# 12055-2-AP, RRID:AB_2301357); FAM134B (Proteintech

Cat# 21537-1-AP, RRID:AB_2878879); TEX264 (Proteintech Cat# 25818-1-AP, RRID:AB_2880272); ATL3 (Proteintech Cat# 16921-1-AP, RRID:AB_2290228); SEC62 (Abcam Cat# ab140644); REEP5 (Proteintech Cat# 14643-1-AP, RRID:AB_2923648); REEP5 (Proteintech Cat# 68119-1-Ig, RRID: AB_2178440); SEC61B (Abcam Cat# ab15576, RRID:AB_301985); Calnexin (Abcam Cat# ab22595, RRID:AB_2069006); p62 (SQSTM1) (MBL International Cat# PM045, RRID:AB_1279301); GAPDH (Proteintech Cat# 60004-1-Ig, RRID:AB_2107436); LAMP1 (Sigma-Aldrich Cat# L1418, RRID:AB_477157); LAMP1 (Enzo Life Sciences Cat# ADI-VAM-EN001, RRID:AB_10630197); mCherry-Tag (Easybio Cat# BE2026, RRID:AB_2936383); ATF4 (Proteintech Cat# 10835-1-AP, RRID:AB_2058600); SEC22B (Synaptic Systems Cat# 186 003, RRID:AB_993020); SAR1B (Proteintech Cat# 15453-1-AP, RRID:AB_2183985); SEC23A (Abcam Cat# ab137582); ATG5 (Cell Signaling Technology Cat# 12994, RRID:AB_2630393); ATG7 (Cell Signaling Technology Cat# 8558, RRID:AB_10831194); ATG9A (Abcam Cat# ab108338, RRID:AB_10863880); ATG14 (Cell Signaling Technology Cat# 96752, RRID:AB_2737056); ATG16L (Cell Signaling Technology Cat# 8089, RRID:AB_10950320); ATG13 (Cell Signaling Technology Cat# 13273, RRID:AB_2798169); Beclin-1 (Cell Signaling Technology Cat# 3495, RRID:AB_1903911); ULK1 (Cell Signaling Technology Cat# 8054, RRID:AB_11178668); FIP200 (Cell Signaling Technology Cat# 12436, RRID:AB_2797913); WIPI2 (abcepta Cat# AP13314a, RRID:AB_11136530); ATG3 (Cell Signaling Technology Cat# 3415, RRID:AB_2059244); PI4KIIA (Proteintech Cat# 15318-1-AP, RRID:AB_2268225); VPS13C (Proteintech Cat# 28676-1-AP, RRID:AB_2881191); SCAP (Abcam Cat# EPR26242-60); p70(S6K) (Cell Signaling Technology Cat# 2708, RRID:AB_390722); Phospho-p70(S6K) (Thr389) Antibody (Cell Signaling Technology Cat# 9206, RRID:AB_330944); Phospho-p70 (S6K) (Thr389) Antibody (Proteintech Cat# 28735-1-AP, RRID:AB_2918197); Phospho-p70(S6K) (Thr229) Antibody (Proteintech Cat# 81592-1-RR, RRID:AB_2935429); Goat Anti-Rabbit IgG (H+L) (Jackson Cat#111-035-003, RRID:AB_2313567); Goat

Anti-Mouse IgG (H+L) (Jackson Cat#115-035-003, RRID:AB_10015289); Goat anti-Rabbit IgG (H+L) Highly Cross-Adsorbed Secondary Antibody, Alexa Fluor 546 (ThermoFisher Cat#A-11035, RRID:AB_2534093); Goat anti-mouse IgG (H+L) Highly Cross-Adsorbed Secondary Antibody, Alexa Fluor 488 (ThermoFisher, Cat#A-11029, RRID:AB_2534093).

Overexpression plasmids and stable cell lines

mCherry-REEP5, HaloTag-REEP5, mCherry-SEC61B, BFP-LC3 were constructed on the PiggyBac transposon vector (RRID:Addgene_210330; RRID:Addgene_210332). LAMP1-YFP was constructed on the pEYFP-N1 vector. ER-DsRed was purchased from Addgene (DsRed2-ER-5, RRID:Addgene_55836). EGFP-REEP5, APEX2-EGFP-REEP5, APEX2-EGFP-SEC61B, EGFP-LC3, were constructed on the pEGFP-C1 vector. APEX2-mCherry-LC3 was constructed on the pmCherry-C1 vector. EGFP-Progerin was constructed on the pMK243 vector (Tet-OsTIR1-PURO) (this plasmid is a kind gift from Dr. Chuanmao Zhang's lab). LAMP1-mStaygold and Calnexin-HaloTag were kind gifts from Dr. Dong Li's lab (Tsinghua University). Stable NRK cell lines expressing the following fluorescent fusion proteins were generated via electroporation, antibiotic selection (hygromycin, G418 sulfate, and puromycin), and FACS sorting: LAMP1-YFP/mCherry-REEP5, APEX2-EGFP-REEP5, APEX2-EGFP-SEC61B, EGFP-REEP5, LAMP1-YFP/HaloTag-REEP5, LAMP1-mStaygold/Calnexin-HaloTag, LAMP1-YFP/mCherry-SEC61B, LAMP1-YFP/ER-DsRed, BFP-LC3/LAMP1-YFP/mCherry-REEP5, EGFP-LC3/mCherry-REEP5, and APEX2-mCherry-LC3.

Generation of KO cell lines

All the knockout cell lines were generated with CRISPR-Cas9 system. Genes of interest were deleted using a modified PX458 plasmid or PX459 plasmid (provided by Wei Guo from Zhejiang University, Haining, China) that contains two single guide RNAs (sgRNAs) coupled with Cas9 nuclease. The sgRNAs were designed at the website of

Broad Institute (https://portals.broadinstitute.org/gppx/crispick/public). Cells transfected with PX458 were seeded into 96-well plates by fluorescence-activated cell sorter selection of EGFP signal expression. Cells transfected with PX459 were selected with puromycin for 7 days and then seeded into 96-well plates by FACS. Genotyping PCR, Western blotting and qPCR were applied for knockout verification.

The targeted genome sequence pairs (two sites slicing) are listed below:

Fam134b-gRNA1: 5'-GCCACTGCATTGCAGAATCA-3'

Fam134b-gRNA2: 5'-CAGAAGAAACGTGAGAGATC-3'

Sec62-gRNA1: 5'-ACAGTTGAATCGAAGATACT-3'

Sec62-gRNA2: 5'-AAATGGGCAAAGGCCAAGAA-3'

Tex264-gRNA1: 5'-GGAGGCTCCTTACCGTCTGG-3'

Tex264-gRNA2: 5'-AGGTGGATGAGCTCAGGTGA-3'

Atl3-gRNA1: 5'-GCTCTGACCCAGAAACTACT-3'

Atl3-gRNA2: 5'-TGAGCTAGAAGAGAGAGCCT-3'

Ccpg1-gRNA1: 5'-CATGCTAATAGCAATCACCA-3'

Ccpg1-gRNA2: 5'-ATTAAAGATGACCTTAACCT-3'

Sar1b-gRNA1: 5'-ATATTTGACTGGATTTACAG-3'

Sar1b -gRNA2: 5'-TCCTTGGATTGGATAATGCC-3'

Sec23a-gRNA1: 5'-AGGACAGGCTCGTACTGAAT-3'

Sec23a-gRNA2: 5'-GATATCCCAGCATATGTAGG-3'

Atg5-gRNA1: 5'-AAGAGTCAGCTATTTGACGC-3'

Atg5-gRNA2: 5'-TCCGTGCAAGGATGCAGTTG-3'

Atg7-gRNA1: 5'-GAACGAGTATCGCCTGGACG-3'

Atg7-gRNA2: 5'-TGACGCCTTCAGTTCGACAC-3'

Atg9a-gRNA1: 5'-AGGCCGAGTACAAACGTGGA-3'

Atg9a-gRNA2: 5'-GAGCTGGGCAAACTCGTCCC-3'

Atg16l1-gRNA1: 5'-AAAAGCACGACGTACCAAAT-3'

Atg16l1-gRNA2: 5'-AGAAGCCAATCGCCTTAATG-3'

Atg13-gRNA1: 5'-GTCGAGCCTGGACAATCACT-3'

1130 *Atg13*-gRNA2: 5'-GATCTCACTCAAGACTTCTG-3'

1131 *Beclin1*-gRNA1: 5'-CCTGGACCGAGTGACCATTC-3'

1132 *Beclin1*-gRNA2: 5'-GGAAGAGGCTAACTCAGGAG-3'

1133 *Ulk1*-gRNA1: 5'-ATCATGTCCCAGCACTACGA-3'

1134 *Ulk1*-gRNA2: 5'-GTGGTGGAAAAATTCATCTG-3'

1135 *Wipi2*-gRNA1: 5'-ACTGCTACTTGGCGTACCCA-3'

1136 *Wipi2*-gRNA2: 5'-GCTCTATATACACAACATCC-3'

1137 *Atg3*-gRNA1: 5'-GTAGACACGTACCATAACAC-3'

1138 *Atg3*-gRNA2: 5'-AGGGGAAGAATTGAAAGTGA-3'

1139 *Pi4k2a*-gRNA1: 5'-TTAGGGTTAAGGTTCCCGTA-3'

1140 *Pi4k2a* -gRNA2: 5'-ATTGACCGAGTAAAGTCCAG-3'

1141 *Vps13c*-gRNA1: 5'-TTAGAACACTGGTACGTCAC-3'

1142 *Vps13c*-gRNA2: 5'-TGGTTAGAAATGCACCATAC-3'

1143 *Npc2*-gRNA1: 5'-CAGGAATAGGGAAGTAGACT-3'

1144 *Npc2*-gRNA2: 5'-AAAGGTGACGTTGACACTGT-3'

1145 *Scap*-gRNA1: 5'-TCTGTCCCGAGCATTCCAAC-3'

1146 *Scap*-gRNA2: 5'-ACCTACCCGCCATTGAGTGT-3'

1147 NRK-*Perk*-KO, NRK-*Sec22b*-KO, NRK-*Atg2*-KO, NRK-*p62*-KO, MEF-*Fip200*-KO,
1148 HeLa-*ATG8*-hexa KO cells were reported before[31,43-46]. NRK-*Atf4*-KO, NRK-*Atf6*-KO,
1149 NRK-*Xbp1*-KO cells were kind gifts from Dr. Dachuan Zhang (Tsinghua University, Li
1150 Yu's lab), NRK-*Atg14*-KO cell line was a kind gift from Dr. Jiayu He (Xinjiang Medical
1151 University, Dr. Na Mi's lab).

1152

1153 **Cell culture**

1154 S2 cells were cultured at 28 °C and 5% CO_2 in Schneider's Drosophila medium
1155 supplemented with 10% fetal bovine serum, 1% penicillin-streptomycin and 1%
1156 Glutamax. MDA-MB-231 cells were cultured at 37 °C and 5% CO_2 in RPMI-1640 high
1157 glucose medium supplemented with 10% fetal bovine serum, 1% penicillin-
1158 streptomycin and 1% Glutamax. THP1 cells were cultured at 37 °C and 5% CO_2 in

RPMI-1640 high glucose medium supplemented with 10% fetal bovine serum, 1% penicillin-streptomycin, 1% Glutamax and 100 ng/mL PMA. The isolated fascia fibroblasts (FFB) and the isolated mouse endometrial stromal cells (MESC) were cultured at 37 °C and 5% CO_2 in DMEM/F-12 medium supplemented with 10% fetal bovine serum, 1% penicillin-streptomycin and 1% Glutamax. The isolated hepatocytes were cultured at 37 °C and 5% CO_2 in Williams E Medium supplemented with 5% fetal bovine serum, 1% penicillin-streptomycin and 1% Glutamax. Other cells were cultured at 37 °C and 5% CO_2 in DMEM high glucose medium supplemented with 10% fetal bovine serum, 1% penicillin-streptomycin and 1% Glutamax.

Immunofluorescence and live cell imaging

For immunofluorescence, cells were grown on confocal dishes and fixed by 4% paraformaldehyde (PFA) at room temperature for 15 min. Then, samples were blocked and permeabilized in PBS containing 0.03% saponin and 10% FBS for 30 minutes at room temperature. Following was incubation with primary antibodies diluted in PBS containing 10% FBS overnight at 4 °C. After washing three times with PBS, cells were incubated with secondary antibodies diluted in PBS containing 10% FBS for 1 h at room temperature in the dark. After final washes with PBS, the samples were imaged with light microscopes.

For live cell imaging, cells were seeded on 3.5mm confocal dishes and monitored with microscopes equipped with a Chamlide environmental incubator system, which maintained the cells at 37 °C and 5% CO_2. Confocal images were acquired with Olympus (FV3000, FV4000) and Nikon (A1HD25, AX R). SIM images were acquired with a Nikon N-SIM microscope equipped with a 100×oil-immersion objective (NA 1.49). Images were reconstructed and analyzed with cellSens software (Olympus), NIS-Elements AR software (Nikon) or ImageJ software (NIH). Z-stack images were reconstructed with Imaris software (Oxford Instruments).

Western blotting and intensities analysis

Cells were solubilized in lysis buffer (2.5% SDS, 50 mM Tris-HCl, pH 7.4) and denatured at 95 °C for 15 min. Following protein quantification with the BCA assay kit (Thermo Fisher, 23227), samples were separated on precast SDS-PAGE gradient gels (Lablead; Epizyme) and electroblotted onto PVDF membranes (Millipore, ISEQ00010). The membranes were blocked in TBST (20 mM Tris-HCl, pH 7.6, 137 mM NaCl and 0.2% Tween-20) containing 5% milk for 1 h at room temperature. Primary antibodies were diluted in Solution I (TOYOBO, NKB-201). After incubation with primary antibodies at 4 °C overnight, the membranes were washed with TBST and then incubated with horseradish peroxidase (HRP)-conjugated secondary antibodies diluted in antibody solution buffer (NCM Biotech, WB100D) at room temperature for 1 h. After final washes with TBST, the membranes were detected and quantified with ChemiDoc Touch Imaging System (Bio-Rad, ChemiDoc MP, RRID:SCR_021693) using Westar ETAC (Cyanagen).

Band intensities were quantified using ImageJ software (NIH). Images were converted to 8-bit grayscale format, and background subtraction was performed using the "Rolling ball radius" method. Proteins of interest were selected using rectangular selections, and lane boundaries were manually defined. The integrated density values were measured and normalized to the corresponding loading control from the same blot. Data from at least three independent biological replicates were analyzed and expressed as fold change relative to the control group.

Quantitative real-time PCR

Total RNA was extracted with MolPure® Flash Cell/Tissue Total RNA Kit (Yeasen, 19221ES50). cDNA was synthesized using a ReverTra Ace qPCR RT Kit (TOYOBO, FSQ-101). Quantitative real-time PCR was performed using 2× T5 Fast qPCR Mix (SYBR Green I) (TSINGKE Biological Technology, TSE202). Primer sequences are provided below:

Ccpg1-1F: 5’-GTCACTGGCGTCTGGAGC-3’

Ccpg1-1R: 5’-TCAGACATTTTTCAGGTCCGAAG-3’

Ccpg1-2F: 5'-CGCGAGCAGGTTGTTGTT-3'

Ccpg1-2R: 5'-TTCAGACATTTTTCAGGTCCGA-3'

Npc2-F: 5'-CCTGAGCCTGACGGTTGTAA-3'

Npc2-R: 5'-CACCACCAGTTTTAGAGAGGG-3'

Srebf1-F: 5'-CTTGACCGACATCGAAGACAT-3'

Srebf1-R: 5'-CCAGCATAGGGGGCATCAAA-3'

Label-free Mass Spectrum

For protein extraction, cells were lysed in 10 volumes of ice-cold lysis buffer (1% sodium deoxycholate, 10 mM Tris-HCl, pH 8.5), immediately boiled at 100 °C for 10 min to inactivate proteases, and sonicated on a pre-chilled (4 °C) non-contact ultrasonicator (30 s on/30 s off, 15 cycles). Lysates were cleared by brief centrifugation, and supernatants were stored at -80 °C until analysis. Protein concentration was determined by BCA assay. Label-free quantitative proteomic analysis was performed by Protein Chemistry and Proteomics Platform (Technology Center for Protein Sciences, Tsinghua University). Proteomic data were acquired on a Thermo Scientific Orbitrap Astral mass spectrometer using data-independent acquisition (DIA) mode. Each group was performed with three biological replicates.

TEM

Cells were cultured on 3.5 mm confocal dishes and fixed in 2.5% glutaraldehyde (GA) (Leagene). The cells were washed with 0.1 M PB buffer (pH 7.2) three times, and post-fixed in 1% osmium tetroxide (Ted Pella)/1.5% K3[Fe(CN)6] in distilled water for 30 min at 4 °C. After three washes with distilled water, the samples were stained with 1% uranyl acetate overnight at 4 °C in the dark. After three washes with distilled water, the cells were dehydrated in a graded ethanol series (50%, 70%, 80%, 90%, 100%, 100%, 100%, for 2 min each on ice, then 100%, 5 min at RT). The cells were infiltrated in Pon 812 (SPI) resin (50%, 67%, 75% for 30 min each, then 100% for 1 h and 100% overnight at RT), and then polymerized at 60 °C for 48 h. Ultrathin sections of 70 nm

1246 were cut by ultramicrotome (Leica EM UC7). After staining with uranyl acetate and
1247 lead citrate, sections were observed under 120 kV transmission electron microscope
1248 (Hitachi, HT-7800).
1249
1250 **CLEM**
1251 Cells grown on gridded glass-bottom dishes (Cellvis, D35-14-1.5GI) were fixed with
1252 4% PFA and immediately imaged with confocal microscope to document the cells of
1253 interest at different magnifications. After that, the cells were post-fixed with 2.5% GA
1254 and prepared for TEM. The steps for preparing ultrathin sections were the same as
1255 standard TEM sample preparation protocols.
1256
1257 **APEX2-TEM**
1258 Cells stably expressing APEX2-EGFP-REEP5 (or APEX2-EGFP-SEC61B, APEX2-
1259 mCherry-LC3) were cultured on 3.5 mm confocal dishes and fixed with 2.5% GA. All
1260 subsequent steps were performed on ice within 1 h of fixation. After three washes with
1261 0.1M PB buffer (PH 7.2), cells were incubated in a freshly prepared solution of 0.5
1262 mg/mL (1.4 mM) DAB tetrahydrochloride (Sigma, D5637) in 0.1M PB buffer (PH 7.2)
1263 for 20 min. Next, a fresh solution containing 0.5 mg/mL (1.4 mM) DAB and 0.03%
1264 (v/v) H_2O_2 was used for the enzymatic reaction. After reaction, the cells were washed
1265 three times with 0.1M PB buffer (PH 7.2). Post-fixation staining was performed with
1266 2% osmium tetroxide for 5 min. Cells were then rinsed three times in distilled water,
1267 and placed in 2% aqueous uranyl acetate (Electron Microscopy Sciences) overnight.
1268 Subsequent steps followed standard TEM sample preparation protocols.
1269
1270 **FIB-SEM**
1271 The resin block was trimmed to expose cells at the surface, then coated with a ~20-nm
1272 gold layer followed by a ~600-nm platinum layer applied perpendicular to the block
1273 face. Imaging was performed on a Helios NanoLab G3 UC scanning electron
1274 microscope in back-scattered electron (BSE) mode using TLD (through-the-lens) and

ICD (in-column) detectors. Each milling cycle used a 30 kV, 0.79 nA ion beam to remove a 10-nm-thick surface layer, and images were acquired with a 2 kV, 0.4 nA electron beam at 8 μs/pixel dwell time.

Sample Vitrification

For sample preparation, a cell suspension with a concentration of approximately 3×10^6 cells/mL was used. 200-mesh copper grids with a continuous carbon film (EMCN, BZ1011125a) were rendered hydrophilic by glow-discharging in ambient air for 25 seconds at 15 mA using a Pelco EasiGlow glow-discharge system. The vitrification process was carried out using a Leica EM GP2 automatic plunge-freezer, operated within an environmental chamber maintained at 25 °C and 75% relative humidity to minimize sample evaporation.

A volume of 3 μL of the suspended cell solution was applied to the carbon-coated side of the glow-discharged grid. To achieve a thin, uniform layer of cells suitable for imaging, 2 μL of buffer was applied to the reverse side of the grid. The grid was blotted from the reverse side for 4-6 s and immediately plunged into liquid ethane cooled by liquid nitrogen, resulting in the vitrification of the sample. Grids were subsequently stored in liquid nitrogen until required for further processing.

Cryo-lamella preparation

Lamellae were prepared from the vitrified cells using a multi-step milling procedure analogous to established protocols[47] with a Helios dual-beam cryo-focused ion beam/scanning electron microscope (cryo-FIB/SEM) (Thermo Fisher Scientific). To balance milling speed with precision and minimize beam-induced sample damage during the milling process, the Ga^{2+} ion beam current at an accelerating voltage of 30 kV was progressively reduced from 0.79 nA for rough milling to 24 pA for final polishing. This procedure yielded lamellae with a final thickness between 100 to 200 nm.

Cryo-electron tomography data collection

Lamellae were imaged on a 300 kV Titan Krios electron microscope (Thermo Fisher Scientific) equipped with a Gatan post-column energy filter. Images were recorded at a magnification of ×53,000, resulting in a calibrated pixel size of 2.4 Å. Tilt-series were collected using the bidirectional tilt scheme over a range of ±60°, with a 2° angular increment. A target defocus of approximately -5 µm was applied, and the total cumulative electron dose for each tilt-series was limited to 120 $e^{-}/Å^{2}$.

Tomogram reconstruction

Following data acquisition, the raw movie frames were processed to correct for specimen drift and beam-induced motion using MotionCor2[48]. The resulting tilt-series were subsequently aligned using patch tracking routine and reconstructed into tomograms by weighted back-projection, employing the IMOD software suite[49]. To enhance the signal-to-noise ratio for visualization and subsequent segmentation, the final tomograms were four-fold binned, and a SIRT-like filter was applied.

Tomogram segmentation and visualization

Three-dimensional segmentation of cellular features within the reconstructed tomograms was performed using Amira (Thermo Fisher Scientific). A semi-automated workflow was employed to generate accurate 3D models of membranes and other structures of interest, which combined automated feature recognition with subsequent manual refinement. Features such as membranes were first identified using threshold-based tools within the software. Each segmented feature was then manually inspected, corrected, and annotated, to ensure anatomical accuracy and remove any artifacts from the automated process. The finalized 3D models were then rendered within Amira for visualization and analysis.

FRAP

Fluorescence recovery after photobleaching (FRAP) experiments were performed using

a Nikon AX R confocal microscope equipped with a 100×oil-immersion objective. After acquiring five prebleach frames (1s intervals), a circular region of interest (ROI; 1 μm diameter) was photobleached with the 488 nm laser at 100% power for 5 s. Postbleach recovery was recorded at 1-s intervals for 60 s. Mean fluorescence intensity within the bleached ROI was quantified at each time point, background-subtracted using an extracellular ROI, corrected for acquisition photobleaching by normalization to an unbleached reference ROI in the same cell, and expressed relative to the mean prebleach intensity (set as 100%). Recovery curves were plotted as mean ± SEM from >20 cells per condition using GraphPad Prism 10 software.

Isolation of primary cells

In this project, we isolated several primary cells from mouse tissues, including lung fibroblasts (LFB), fascia fibroblasts (FFB), dermal fibroblasts (DFB), hepatocytes, mouse embryonic fibroblasts (MEF) and mouse endometrial stromal cells (MESC), following previously described protocols[50-54].

Human dermal fibroblasts (HDF) from healthy donors and HGPS patients were obtained from Dr. Chuanmao Zhang's lab, as previously reported[55].

***In vitro* reconstitution**

S150 cell extract preparation: Cells were harvested and washed with cold PBS, and resuspended in 2× cytosol buffer (50 mM Hepes-KOH, 50 mM KOAc, 2.5 mM MgCl2, 250 mM sucrose, PH 7.4) containing protease inhibitors. Lysis was performed by mechanical disruption (25G needle or homogenizer) until >80% efficiency was confirmed by typan blue (Solarbio Life Sciences, C0040) staining. The lysate was centrifuged sequentially at 1,000×g for 10 min and 120,000×g for 20 min at 4 °C. The supernatant was then ultracentrifuged at 150,000×g for 1 h at 4 °C. The final S150 supernatant was acquired, protein concentration was determined by BCA assay (~10 mg/mL), and aliquots were flash-frozen in liquid nitrogen and stored at -80 °C.

We have tried several protocols for *in vitro* reconstitution, the most efficient is described

below. After incubation with 200 μM oleic acid for 20 h, cells grown on 3.5 mm confocal dishes were treated with reaction buffer (25 mM Hepes-KOH, 25 mM KOAc, 1.25 mM MgCl2, 125 mM sucrose, PH 7.4) containing 40 μg/mL digitonin and protease inhibitors alone (mock group), or additionally supplemented with 50% S150 and an energy system (1 mM ATP, 0.5 mM GTP, 20 mM creatine phosphate, 0.2 mg/mL creatine kinase) (all group). Both groups were incubated at 30 °C for 6-8 h to allow reconstitution, then fixed with 2.5% GA for TEM analysis. Cell death was confirmed using Apotracker and PI, and plasma membrane permeabilization was assessed with Cy5.

Negative staining TEM

A droplet of S150 or resuspended P150 was deposited onto copper grids for 5 minutes. Excess sample was blotted with filter paper. The grid was promptly washed with a droplet of double distilled water (ddH_2O), stained with 1% uranyl acid for one minute, and washed twice with droplets of ddH_2O. Residual water was blotted using filter paper, and the grid was air-dried before imaging by transmission electron microscopy (TEM).

Statistical analysis

Normality was assessed using a Kolmogorov-Smirnov test. Statistical analyses were conducted with GraphPad Prism 10 using an unpaired two-tailed Student's t-test. Sample sizes were determined empirically without a priori statistical calculations, and all acquired data were retained for analysis. Error bars indicate mean ± SEM. *P<0.05, **P<0.01, ***P<0.001, ****P<0.0001, ns, not significant.

Acknowledgements

This research was supported by Tsinghua University Dushi Program (grant no. 20251080019), the Ministry of Science and Technology of the People's Republic of China (grant no. 2024YFA1307301, 2024YFF1502900), the National Natural Science Foundation of China (grant no. 32030023, 92354306, and 32330025), Tsinghua-Toyota

Joint Research Fund (grant no. 20233930058), and Scientific and Technological Innovation Project of China Academy of Chinese Medical Sciences (grant no.CI2023C024YL). We sincerely show our gratefulness to the State Key Laboratory of Membrane Biology for confocal microscopy imaging and facility support. We are grateful to Yan Yang, Chenguang Zhao, Yanfei Hu, Qian Li from the Cell Biology Facility affiliated with the Center of Biomedical Analysis, Tsinghua University, for technical assistance and equipment support. We thank SLSTU-Nikon Biological Imaging Center for microscopy imaging and facility support. We thank Dr. Dachuan Zhang (Tsinghua University, Dr. Li Yu's lab) for providing NRK-*Atf4*-KO, NRK-*Atf6*-KO, NRK-*Xbp1*-KO cells. We thank Dr. Jiayu He (Xinjiang Medical University, Dr. Na Mi's lab) for providing NRK-*Atg14*-KO cells. We thank Dr. Du Feng from Guangzhou Medical University for providing HeLa-*ATG7*-KO cells and its wildtype HeLa cells. We thank Dr. Michael Lazarou from Monash University for providing HeLa-*ATG8*-hexa KO cells and its wildtype HeLa cells. We thank Dr. Xiangyang Wang from Dr. Chuanmao Zhang's lab (Peking University, Kunming University of Science and Technology) for providing human dermal fibroblast (HDF) cells. We thank Dr. Zheng Jiang from Dr. Anming Meng's lab (Tsinghua University) for providing mouse zygotes. We thank Dr. Wenfeng Fu from Dr. Dong Li's lab (Tsinghua University) for providing the LAMP1-mStaygold and the Calnexin-HaloTag plasmids. We thank Dr. Xiong Ji from Peking University for proving the pMK243 (Tet-OsTIR1-PURO) plasmid.

Author contributions

L.Y. and D.L. conceived and designed the study. L.Y. supervised the project and wrote the manuscript. D.L. performed cell biology, molecular biology, biochemistry and EM experiments. R.Z. performed Cryo-ET experiments. W.S., D.Z. and Y.Y. participated in generation of knockout cells. X.S. and H.Z. isolated primary cells from mouse tissues. All authors reviewed and approved the final manuscript.

Declaration of interests

1420 L.Y. is the scientific founder of Migrasome therapeutics Ltd. All other authors declare
1421 no conflicts of interest.